UNIVERSITY OF TWENTE.

**Faculty of Electrical Engineering,
Mathematics & Computer Science**

SDR-based concurrent multi-band event matching using bistatic Wi-Fi “radar”

Feifan Zhang

M.Sc. Thesis
January 2023

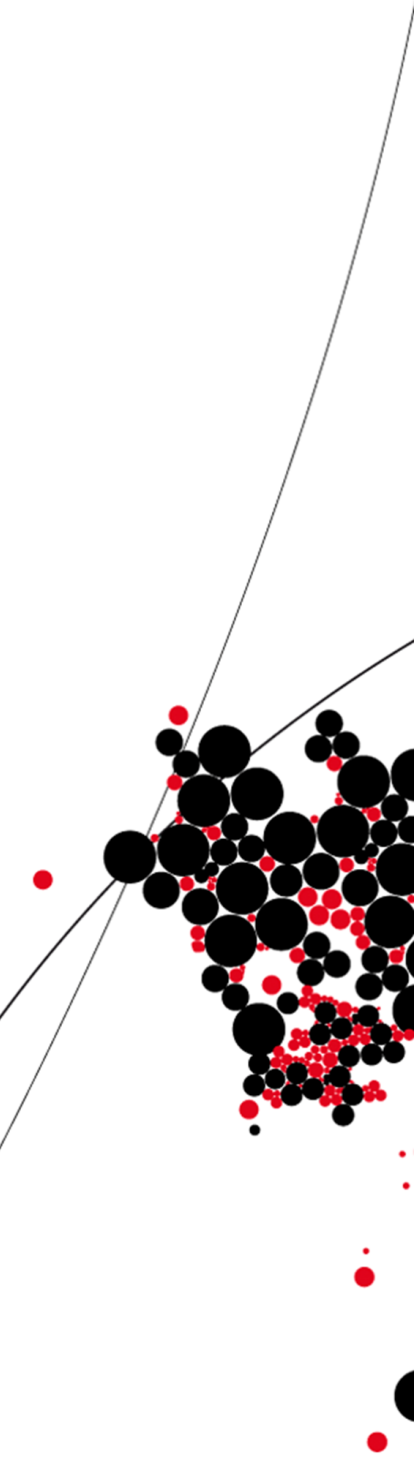

Supervisors:
assoc.prof.dr.ir. A.B.J Kokkeler,
asst.prof.dr. Yang Miao,
MSc. Zaher Mahfouz,
MSc. Hadi Alidoustaghdam,
asst.prof.dr. Yanqiu Huang

Radio System Group
Faculty of Electrical Engineering,
Mathematics and Computer Science
University of Twente
P.O. Box 217
7500 AE Enschede
The Netherlands

ACKNOWLEDGMENTS

Thanks to my family for all they have done for me, especially regarding my decision to continue to complete my studies in the RS group.

I am extremely thankful to my graduation committee members: Assoc.Prof.A.B.J Kokkeler, Asst.Prof.Yang Miao, Zaher Mahfouz, Hadi Alidoustaghdam and Asst.Prof. Yanqiu Huang for their advice and comments.

My gratitude also goes towards my daily supervisors and RS group members, for their patient help in the form of valuable suggestions and information, providing the necessary equipment as well as integrating me into the RS group.

In the end, I am able to appreciate my study advisor, E.T. Wassink-Kamp. She has given me lots of help in both study and life.

Summary

Due to the rapid development of wireless networks, as well as the similarities in signal processing algorithms, devices, and system architectures, Joint Wireless Communications and Radar Sensing (JCAS) becomes a new feature of future systems. Also because of the broad deployment and low cost of wireless communication infrastructure, ubiquitous Wi-Fi signal is used for wireless sensing. It uses MIMO-OFDM technology with high spectral efficiency, strong multiplexing and anti-interference ability, which can carry Channel State Information (CSI) very well. By signal processing techniques, the electromagnetic wave information, containing the radio interactions with the environment and sensing target, can be retrieved for localization, identification and tracking.

As a significant component of identification, the requirements for Human Activity Recognition (HAR) are rising in the fields of healthcare, entertainment and leisure. Most of the CSI-based solutions obtain CSI from commercial Wi-Fi devices, e.g, network NIC cards. But it can't provide fine-grained CSI and also causes extra noise. In contrast, Wi-Fi radar, which uses specific Wi-Fi device Software-Defined Radio (SDR), supplies rich CSI. The wireless systems are controlled and operated by software without any hardware modification, bringing flexibility and cost efficiency.

In order to identify HAR precisely, we propose a double-band event matching Wi-Fi HAR sensing system at 5.8GHz and 900MHz. Unlike existing schemes that only use single-band, dual-band combines high Doppler resolution of high-frequency signals and high amplitude sensitivity of low-frequency signals, which can extract Doppler and amplitude information separately to improve event-matching accuracy. Firstly, an SDR-based dual-band Physical Layer (PHY) MIMO-OFDM transceiver is designed. It contains clock/time/frequency/phase synchronization, channel estimation and MIMO equalizer algorithms. Then, we implemented the simulator on MATLAB/Simulink platform to validate the communication and sensing performance of the RX demodulator and SDR. After that, the measurement is applied to different scenarios with various events.

For the signal processing process, after extracting the original IQ samples, the noise effect is reduced and the first-order difference reduces the multi-path effect caused by environmental variation. When the preprocessed CSI is completed, a

fast Fourier transform obtains the amplitude and Doppler information. Finally, the classification of human activities is done based on the maximum Doppler shift and the time difference between adjacent amplitude peaks.

Experimental results show that a maximum event matching accuracy of 98.54% can be achieved under dual-band, 1.5Mbps sampling rate and orthogonal TRx antenna array layout. The average matching accuracy of the three sampling rates selected in the study can only reach 86.61%, indicating that the currently selected sampling rate is not the best choice. Orthogonal TRx antenna array layout has better event-matching accuracy than parallel antenna layout.

Contents

List of acronyms

JCAS	Joint Wireless Communications and Radar Sensing
RSS	Received Signal Strength
CSI	Channel State Information
SDR	Software-Defined Radio
OFDM	Orthogonal Frequency Division Multiplexing
MIMO	Multiple Input Multiple Output
SC	Subcarriers
USRP	Universal Software Radio Peripheral
RF	Radio Frequency
TX	transmitter
RX	Receiver
UAV	Unmanned aerial vehicle
IQ	In-phase and quadrature
MSE	Mean Square Error
PHY	Physical Layer
UWB	Ultra Wide Band
HAR	Human Activity Recognition
BER	Bit Error Rate
ML	Maximum Likelihood
DSP	Digital Signal Processing

STF Short Training Field

LTF Longer Training Field

FFT Fast Fourier Transform

CP Cyclic Prefix

ICI Inter Carrier Interference

CFO carrier frequency offset

Chapter 1

Introduction

As a widely used wireless network transmission technology, Wi-Fi communication applies in fields of consumer electronics, military, aerospace etc. Compared with wired communication, Wi-Fi does not require wiring and additional equipment. It has the advantages of high flexibility, easy operation and deployment, which is very suitable for the requirement of mobile users. Compared with the cellular network, Wi-Fi has more stable performance, low cost and energy consumption, which is suitable for the long-term utility of short-distance multi-device.

The advantages of Wi-Fi have promoted the full coverage of Wi-Fi networks and the popularization of Wi-Fi devices, which expands the range of applications for Wi-Fi. Unlike device-based sensing approaches, there is unnecessary to put any sensing equipment on the perception targets and no need to equip expensive radar. As a Radio Frequency (RF) signal, Wi-Fi records the characteristics of the physical space it traverses during transmission, that is, the state of the transmission channel. Therefore, it can be used for sensing. Compared with dedicated radar signals or even Ultra Wide Band (UWB) signals, Wi-Fi has great advantages in universality. Wi-Fi signals can be directly deployed to existing devices without additional sensors and specific environmental requirements. User privacy is also guaranteed. But these devices are not precise enough and even create extra noise from devices. For fine-grained motion sensing, Wi-Fi can also use dedicated RF equipment, that is, use SDR and Universal Software Radio Peripheral (USRP) to extract In-phase and quadrature (IQ) samples to obtain environmental status [1]–[3].

Currently, Wi-Fi sensing utilizes two important physical layer properties: Received Signal Strength (RSS), CSI. RSS refers to the received signal strength, which is inversely proportional to the signal propagation distance and can measure the quality of the channel link. Some RSS-based methods have been used for Unmanned aerial vehicle (UAV) navigation [4], vehicle detection [5], robot/human localization [6] and behavior classification [7], such as sitting, standing, walking, etc. However, RSS represents the average value of the received signal, which reflects the coarse-grained

channel information, is susceptible to multi-path effects and has low sensitivity. In contrast, CSI has amplitude and phase (fine-grained) information. With the proper RF equipment, small channel variations can be identified.

Because of Wi-Fi signals' excellent communication and sensing capabilities, JCAS is the tendency of future system development. This research concerns the sensing systems utilizing SDR platform with CSI.

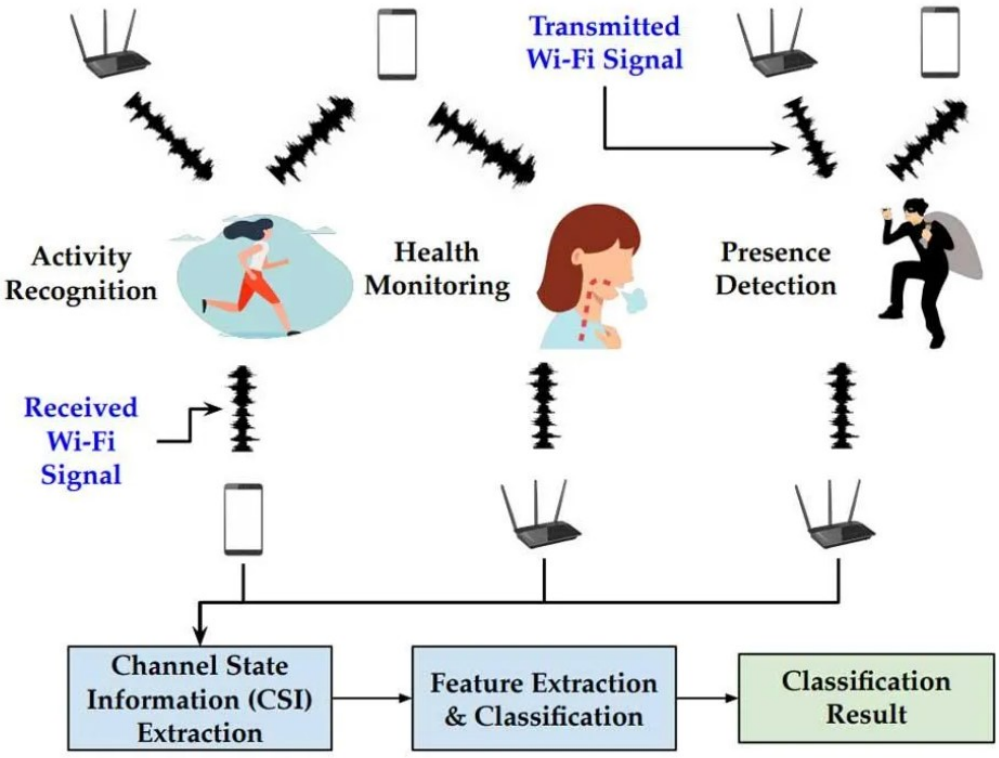

Figure 1.1: Overview of Wi-Fi sensing [8]

1.1 Background

1.1.1 IEEE 802.11 Standards

The thesis adopts 802.11ah and 802.11ac standards as physical layer structure references in two frequency bands respectively. 802.11ah is a sub-GHz Wi-Fi standard that utilizes the LICENSE-EXEMPT band. It started in 2010 and stopped amendment in 2017. And 802.11ac operates in 5.8GHz unlicensed band. It was developed in 2008 and the first version was published in 2013 [9], [10]. Table 1.1 shows the features of the 802.11ah/ac standard,

technology	Frequency	modulation	channel width	range	MIMO	FFT
802.11ah	900MHz	BPSK to 256QAM	1,2,4,8,16MHz	up to 1000m	up to 2x2	32,64,128,256,512
802.11ac	5.8 GHz	BPSK to 256QAM	20,40,80,160MHz	up to 92m	up to 4x4	64,128,256,512

Table 1.1: 802.11ah/ac characteristics

1.1.2 MIMO& OFDM

Multiple Input Multiple Output (MIMO) technology is a system that uses multiple antennas at both TX and RX to form multiple channels (see in Figure 1.2). It utilizes space resources to achieve reliability and availability, which enhances spectrum efficiency and system coverage range. Each channel experiences independent fading. For communication, multiple antennas increase diversity to overcome channel fading. When the same data is sent through the different TX antennas, comparing the data obtained by different receiving antennas can reduce the average Bit Error Rate (BER). For sensing, different channel fading corresponds to different CSI. By collecting CSI under different channels simultaneously, the channel state can be perceived comprehensively.

When using MIMO, OFDM is usually selected as the modulation scheme. The most important reason is that the OFDM signal has high interference robustness. It's because the OFDM signal is composed of many orthogonal sub-channels in the frequency domain (Figure 1.3). It uses a Subcarriers (SC) for modulation on each sub-channel and transmits each subcarrier in parallel. Although for the integrated OFDM signal, its frequency response curve is not flat, for each sub-channel, the channel is relatively flat. Therefore, narrow-band transmission is carried out on each sub-channel and the signal bandwidth is narrower than the corresponding bandwidth of the channel, which eliminates the interference between signal waveforms [11]–[13].

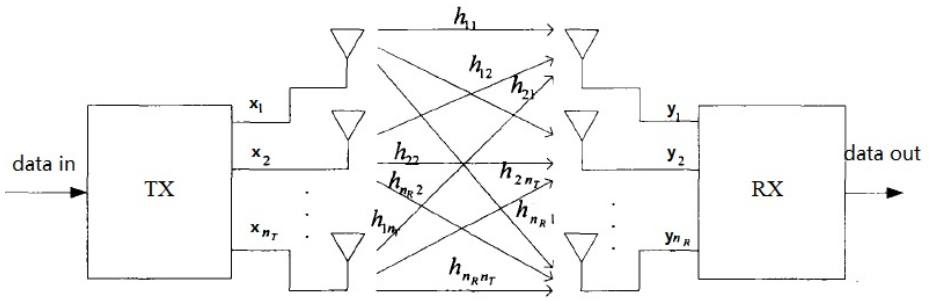

Figure 1.2: MIMO Spatial Multiplexing

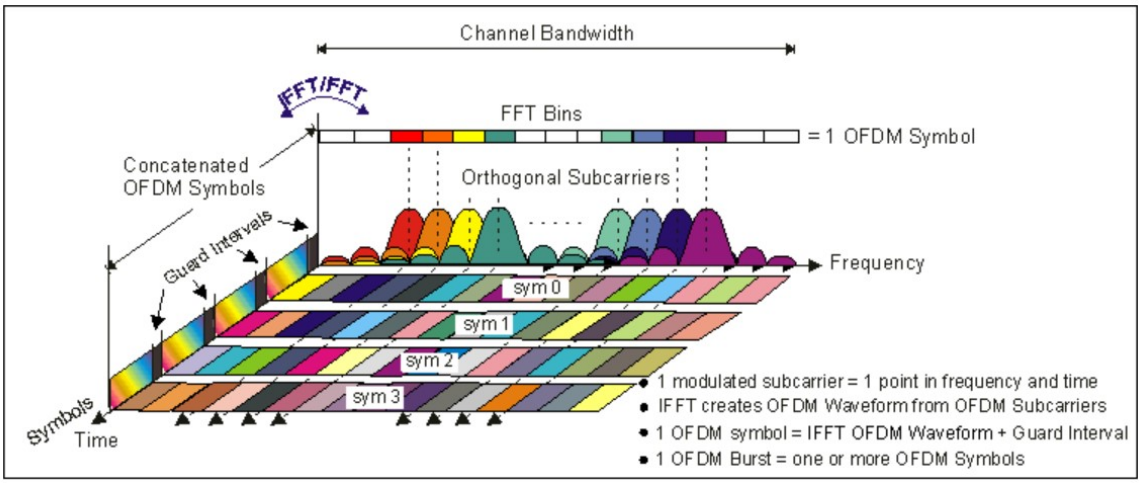

Figure 1.3: An OFDM signal in frequency and time domain [13]

1.1.3 Channel State Information & Delay-Doppler-Angular Domain Information Retrieval

CSI characterises the whole propagation process between the TX and RX transmission. According to 802.11 ah/ac, CSI can be obtained in each OFDM SC. Multi-path effects produce different amplitude attenuation, phase shift and time delays in CSI. Each CSI entry represents the time-variant impulse response of each path. Thus, the RX signal is expressed like [3]

$$Y(t,f) = X(t,f) \times H(t,f) + N_w \tag{1.1}$$

where $X(t,f)$ is the TX signal, N_w refers to an additive white Gaussian noise vector and CSI is formulated as [3]

$$H(t,f) = e^{-j2\pi\Delta f t} \sum_{pt=1}^{N} a_i(t,f) e^{-j2\pi f \tau_{pt}(t)} \tag{1.2}$$

where N denotes the number of propagation paths,$a_{pt}(t,f)$ is the amplitude attenuation factor and $\tau_{pt}(t)$ is the propagation delay of the pt_{th} path, Δf is the frequency offset because of the local oscillators difference between TX and RX, f is the carrier frequency.

Because TX, RX and any variations between TX and RX will affect the amplitude $|H|$ and phase $\angle H$ of CSI [14], CSI can record environmental characteristics, which is the foundation of Wi-Fi sense.

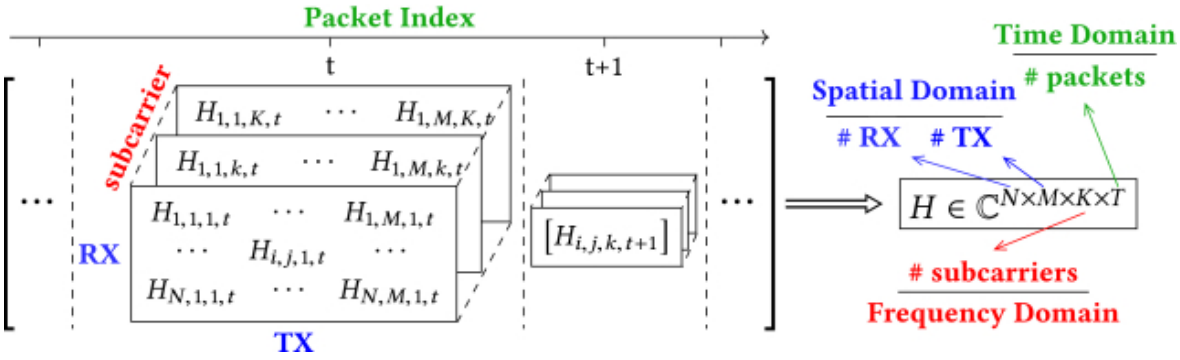

Figure 1.4: MIMO-OFDM CSI matrics channels in time domain [14]

1.2 Related works on Wi-Fi sensing

Wi-Fi sensing systems are divided into three broad categories: 1) HAR (large and small scale); 2) object sensing; 3) localization [4], [6]. HAR refers to the process of recognizing specific human movements or actions, ranging from large-scale movements, such as daily activity recognition [2], [15]–[23], fall detection [24]–[26], human recognition [27], [28] and human presence detection [29]–[32] to small-scale movements, like vital signs [29], [33]–[35] and finger gestures [3], [19], [36]–[38]. Object sensing refers to the perception of the external or internal structure and the class of static objects. For example, distinguishing person and cylinder in NLOS scenarios [39]. Localization is the process of seeking the location of an object in space, including a series of changes in the position of the tracked target [33], [40]. Current typical researches on Wi-Fi sensing with CSI for HAR are as follows

Studies surge in commercial hardware to collect CSI to identify human activities. [20] uses two PCs equipped with NICs to extract CSI values, 5 different human motions were identified at 24 locations between the transceivers. [21] developed a gesture recognition system which is independent of the user position. In addition to the above coarse-grained recognition, CSI also offers great potential for detecting fine-grained motions, as it can capture small motions effects on SCs. [22] proposed WiKey, which classifies small hand and finger movements in typing by exploiting changes in CSI keystroke recognition. However, the accuracy of all the above studies is unsatisfactory because NIC only reports the channel matrix for 20 to 30 SCs magnitude without any phase information. It's difficult to handle sensitive environmental variation.

In order to use phase information and flexibly adjust OFDM structure, some studies use specialized research equipment, most of which are USRP. [3] used USRP to build a gesture recognition system named WiGrus, which modified OFDM frame structure and can identify gestures in LOS and NLOS scenarios. [23] identified 7 human activities based on a Deep Gated Recurrent Unit (DGRU) in USRP, which

requires complex analog circuits and facilities. Besides amplitude and phase information, the Doppler shift also assists recognize human motion. [36] also used USP to capture the Doppler shift to recognize 9 human motion gestures. It works in 3 different scenarios: LOS, NLOS and through the wall. Compare with using commercial hardware, using USRP significantly improves the HAR accuracy.

1.3 Motivation and Objectives

1.3.1 Motivation

Compared with traditional HAR systems that use sensing devices and radars, Wi-Fi sensing systems do not require users to wear motion sensors, nor do they need to cost a lot and there are no privacy leaks and action inconvenient problems. Compared with commercial Wi-Fi hardware, Wi-Fi sensing systems based on specialized hardware devices (such as SDR) can make full use of all available SCs of Wi-Fi signals and use hardware programming, MIMO-OFDM transceiver algorithms to correct frequency and phase offset, providing more complete and reliable channel information.

As mentioned before, the parameters contained in the wireless signal are RSS and CSI. Both of them are commonly used in HAR. However, existing RSS-based techniques suffer from the following serious flaw: RSS varies greatly with the environment, which may lead to error detection. While CSI is temporally stable in static environments and behaves differently in variable scenarios. Therefore, CSI is suitable for identifying time-varying human activities.

Analyzing the current research, it can be found that the existing Wi-Fi sensing systems are almost all applied to a single frequency band. The only one that adopts multi-band sensing is used for estimating distortion parameters and extending the bandwidth [41]. This technique has been used for radar sensing [42]–[44]. In addition, the use of multiple frequency bands can add more functions, such as one frequency band for sensing and another frequency band for communication [42]. Moreover, the application of dual-band has the potential to solve the radar shadow effect. The target is invisible to the high-frequency signal when being locked by the mask target, the lower frequency has a chance to pass through the mask target and reach the shadow target [15]. Therefore, integrating the CSI of the two frequency bands has the potential to obtain a more accurate perception. These advantages can also be applied to Wi-Fi sense.

In order to apply the advantages of dual frequency bands as much as possible, a high frequency and a low frequency can be selected. Under different configurations, the two frequency bands will generate different types of information, and more

comprehensive and accurate CSI can be obtained. Under the same configuration, high-frequency signals have higher Doppler resolution, while low-frequency signals have higher amplitude sensitivity. Based on the extracted amplitude and Doppler information, human activities can be more accurately identified.

Therefore, comprehensive above analysis, this research adopts bistatic dual-band SDR-based equipment to design a Wi-Fi sensing system with CSI, including amplitude and Doppler shift information.

1.3.2 Objectives

The main purpose of this thesis is to design a concurrent double Wi-Fi band event-matching system that

(i) utilizes two BladeRF 2.0 xA9 boards (SDR device) to implement a bistatic 2x2 MIMO-Orthogonal Frequency Division Multiplexing (OFDM) prototype

(ii) matches different human events in orthogonal and parallel TRx antenna array layouts

The main contributions of our works are :

1. we are the first to utilize both the maximum Doppler shift and peak-to-peak amplitude difference from CSI for human event matching.
2. we present SDR-based double-band Wi-Fi sensing.
3. we build a 2X2 MIMO bistatic ”radar” on the MATLAB platform.
4. investigates the parameters which affect the identification ability, including dual-band, sampling rate and TRx antenna array layout.

1.4 Thesis organization

The structure and arrangement of the thesis are as follows:

Chapter 2 states the PHY design of the concurrent double band 2x2 MIMO-OFDM prototype for transmitter (TX) and Receiver (RX). Besides, it introduces the algorithm of the Wi-Fi sensing process and testbed validation.

In Chapter 3, the measurement setup is presented. After that, it introduces events and scenarios of actual measurement.

Chapter 4 initially gives the performance metrics for HAR. Then it shows some examples of real-life measurement results. Finally, the impact of the sampling rate and the antenna layout on event matching are discussed.

In Chapter 5, conclusions and recommendations are given.

Chapter 2

Concurrent dual-band MIMO-OFDM Prototype

This chapter starts with an introduction to the Wi-Fi sensing process with signal processing methods, then, it states the SDR and SDR Development kit (MATLAB/ Simulink) hardware interface and toolbox. After that, the SDR platform(BladeRF) and antenna specifications are given. Later, it presents the OFDM frame structure and related parameters. Moreover, the transceiver design is shown. Finally, based on the MIMO-OFDM testbed, it gives validation.

2.1 Wi-Fi Sensing and CSI Processing Overview

Figure2.1 shows the flow chart of the whole Wi-Fi sensing process. The raw IQ samples come from synchronized RX. Correct and high-performance RX is the premise of extracting CSI features. Section2.2.1 to Section2.4 are used for processing IQ samples. This section introduces some methods to migrate CSI degradation from environmental and hardware internal noise effects.

Completing preprocessing IQ samples, data is extracted in frequency and time domains. Combining Doppler and amplitude/phase changes under different events in dual frequency bands can accurately identify human activities.

2.1.1 Multipath Mitigation

In Figure2.2, the received signal is the sum of the line-of-sight(LOS) path, non-user reflected paths from static objects and dynamic reflected paths caused by human motion in an indoor environment [45]. The former, called non-user reflected paths, including LOS paths and paths reflected from static objects, is resilient to human movements, and only relates to the static environment [3]. Let H_nf represent the

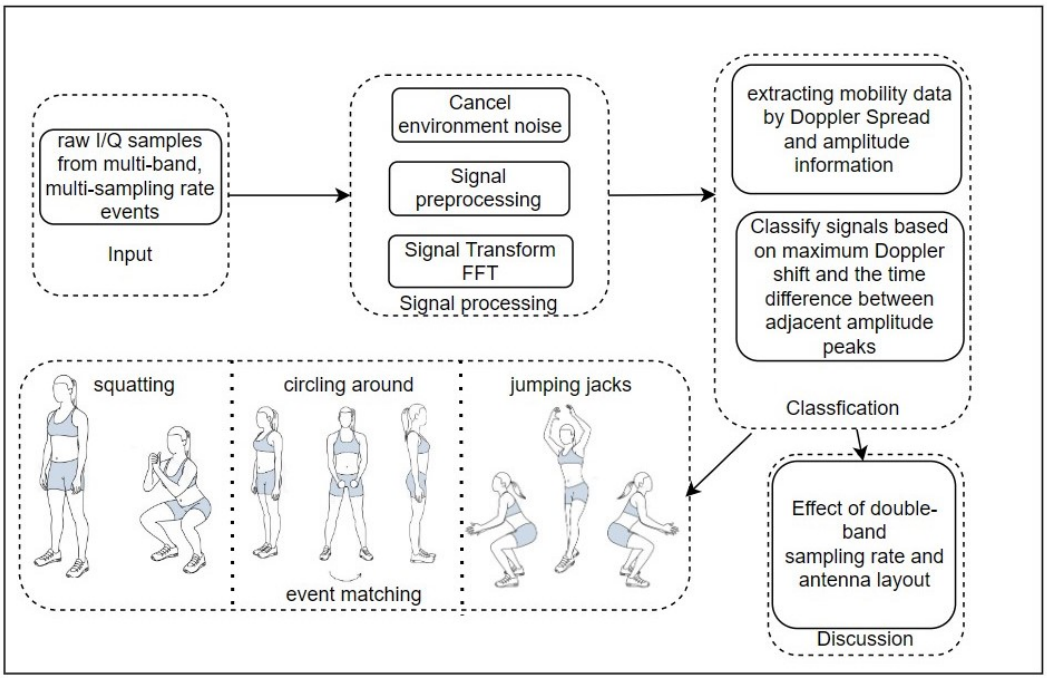

Figure 2.1: Wi-Fi sensing Flow chart

aggregated CSI of all non-user reflected paths. The later one named the user reflected paths, includes the component reflected directly from the human body to the RX and the component reflected from the human body and then passing through the environment to reach the RX. Among them, the second item has experienced multiple reflections in the environment which caused great attenuation, so it can be ignored. Thus, the first component can be regarded as the user-reflected paths, its CSI aggregation can be written as $H_u(t, f)$, it's formulated as:

$$H_u(t, f) = \sum_{\kappa \in U}^{N} a_\kappa(t, f) e^{-j2\pi f \tau_\kappa t} \tag{2.1}$$

where U is a collection of user-directed reflection paths. After frequency and phase synchronization, there is no frequency offset and phase offset, that is $e^{-j2\pi\Delta f t} = 1$. Thus equation1.2 can be rewritten as

$$\begin{aligned} H(t, f) &= e^{-j2\pi\Delta f t}(H_u(t, f) + H_n f) \\ &= H_u(t, f) + H_n f, \end{aligned} \tag{2.2}$$

Then differentiate the above equation with respect to t. Because $H_n f$ is a time-independent term, which can be removed by differentiation. The equation becomes

$$dH(t, f) = dH_u(t, f) \tag{2.3}$$

Therefore, the CSI value only keeps the human directly reflected component, which mitigates multipath effects and promotes the robustness of our system to environmental changes.

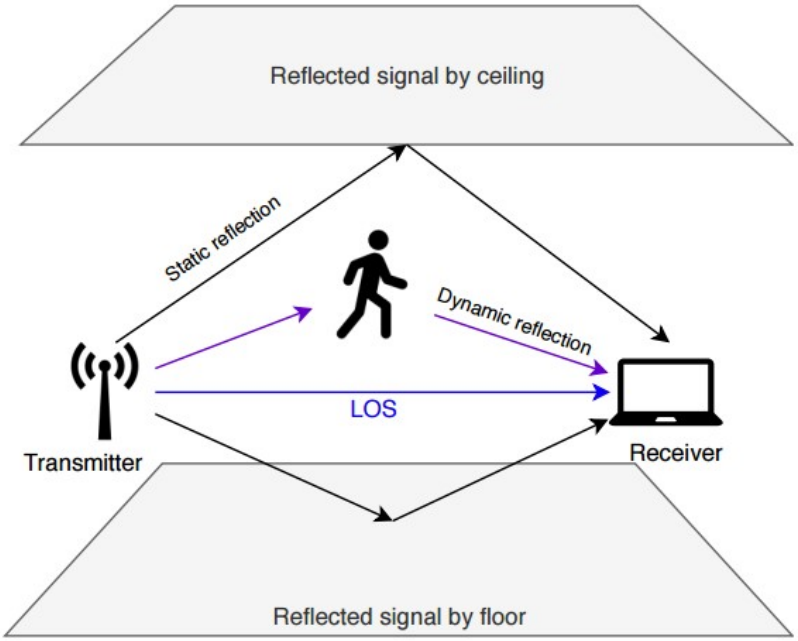

Figure 2.2: HAR paths in an indoor environment [45]

2.1.2 CSI Preprocessing

After eliminating the environmental noise, the CSI signal needs to be pre-processed, that is, adding a frame window. In this way, the computation is reduced and the completeness of recorded information is guaranteed. The window size is determined by the minimum identifiable activity. In this study, 4 times the frame length is selected as the sliding window in the 5.8GHz frequency band and 2 times the frame length in the 900MHz frequency band.

2.1.3 Doppler shift extraction

Doppler shift is the frequency variation caused by the movement between the TX and RX [38]. With the motion of the human body, the related speed between the RX and the human is varied. We can observe the speed or frequency shift of different human activities relative to the RX to identify different events.

In general, the Doppler shift generated by an object moving toward/away RX with

a speed of v and an angle of ϕ is [46]

$$f_{Doppler} \propto \frac{2vf_c cos\phi}{c} \tag{2.4}$$

where c is the light speed, f_c is the carrier frequency. It means higher carrier frequency results in a higher Doppler shift in the same case. The faster the speed, the higher the Doppler shift. Therefore, concurrent transmission in two different frequency bands has different Doppler shifts. And Higher frequency band provides more abundant Doppler information. The relationship between the CSI($H(t, f)$) and Doppler transform function ($B(v, f)$) is in Figure2.3, the equation can be written as

$$B(v, f) = \sum_{\kappa \in U}^{N} H_u(t, f) e^{-j2\pi f \tau_\kappa} \tag{2.5}$$

where κ and U are defined in section 2.1.1, N is the length of $H_u(t, f)$.

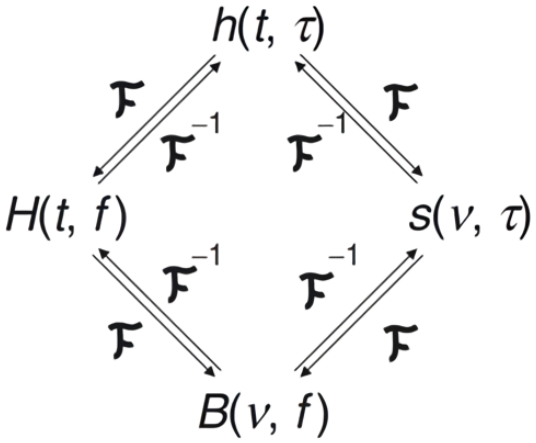

Figure 2.3: Conversion relationship between Doppler frequency shift and CSI [46]

2.2 SDR

SDR is a term to refer to radio systems with almost all its functionality done in software, instead of hardware as it is commonly found in most of the RF applications in recent times.

An ideal SDR, as shown in Figure 2.4, would have an RF Front End only consisting of a power amplifier and high-speed Analogue to Digital converter. Hence, the remaining physical layer functions such as modulation, synchronisation or encoding are done using Digital Signal Processing (DSP).RF Front End is in an SDR platform(e.g. BladeRF),DSP is deployed on an SDR development kit and SDR software(e.g. MATLAB/Simulink).

SDR systems are expected to work in a wide range of the frequency spectrum and to perform various operations as a dedicated hardware implementation would have. Some involved fields for SDR are [1]:

- Development and study

  SDR is used for the analysis of communication protocols and sensing in the physical and data link layers.

- Military Communications

  In the direction of satellite communication and radar detection, the radio can be directly manipulated in modulation and demodulation and signal encryption through software.

- Civil Communications

  SDR only change software instead of hardware, which could minimize the cost of infrastructure.

- Test and Analysis

  SDR is widely used in analysing the signal waveform, spectrum and applications, which can rapidly test and verify prototypes.

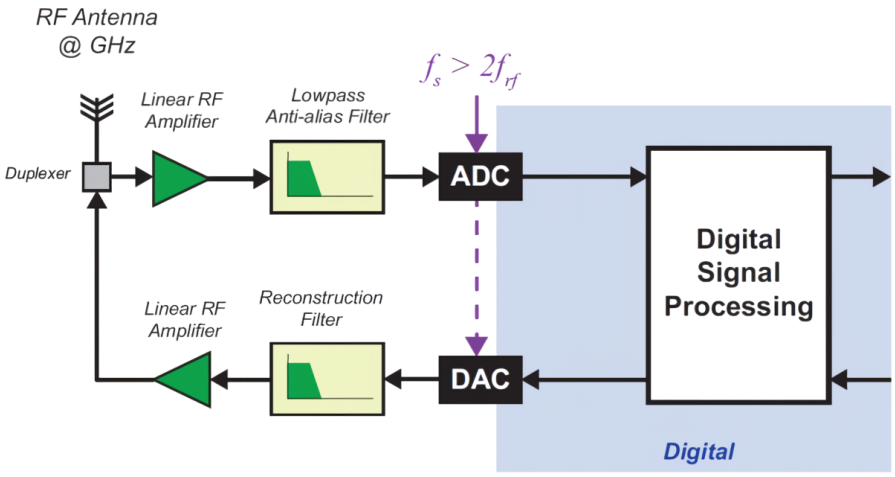

Figure 2.4: Ideal SDR block diagram [47]

2.2.1 SDR Selection

The main effect of the SDR platform is to convert between analog signals and digital signals. The left part of Figure 2.4 illustrates the block diagram. Many SDR units are

SDR	Ettus B210	Hack RF	RTL-SDR	LimeSDR mini 2.0	BladeRF 2.0
Frequency	70 MHz - 6 GHz	1 MHz - 6 GHz	22 MHz - 2.2 GHz	10MHz-3.5MHz	47MHz-6GHz
RF bandwidth	61.44 MHz	20 MHz	3.2 MHz	40 MHz	61.44MHz
Duplex	full	half	N/A	full	full
MIMO	2x2	1x1	0x1	1x1	2x2
TX power	10dBm	15dBm	N/A	10dBm	8dBm

Table 2.1: SDR comparison table [48]–[50]

available to buy today, the vast majority of them are meant for research and industrial applications with companies such as Ettus Research and National Instruments being two of the most popular SDR manufacturers.

Table 2.1 shows the current common SDR. According to the research objective(2x2 MIMO, support 802.11 ah/ac standard, full duplex), only two of the listed SDRs satisfied all requirements. They are Ettus B210 and BladeRF 2.0 xA9(see Figure 2.5). The latter SDR is the one selected as the B210($ 2745) has a higher cost than BladeRF 2.0($ 860).

The BladeRF is a mid-tier SDR containing a 301KLE Cyclone V FPGA, an Analog Devices AD9361 RF transceiver and a Cypress FX3 USB3.0 SuperSpeed controller. It supports 2x2 MIMO with a maximum 60dB gain in TX and 90dB gain in RX. And it can also be linked to another BladeRF and synchronize their clock to achieve 2x2x2 MIMO(see Figure 2.6). Finally, it has support for C/C++, Python, GNU-Radio and MATLAB/Simulink (2x2 MIMO).

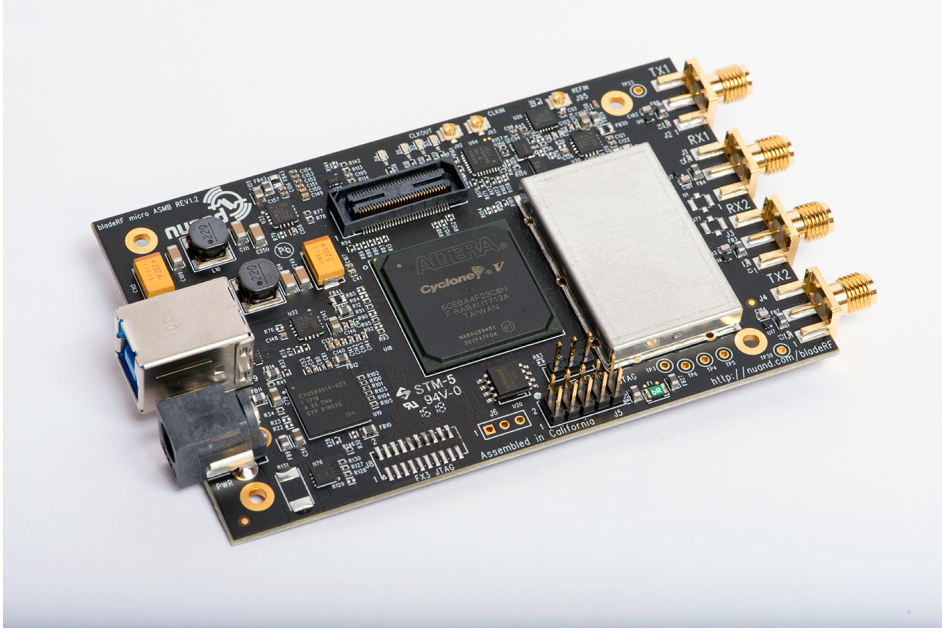

Figure 2.5: Nuand bladeRF 2.0xA9 SDR platform [48]

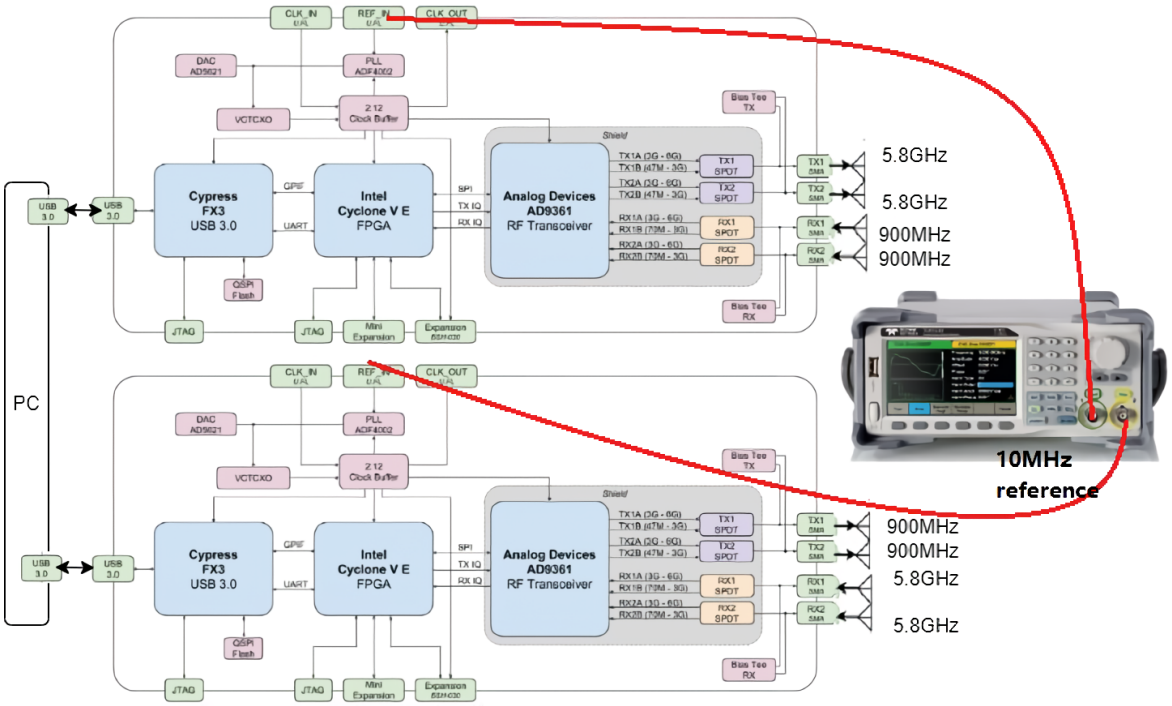

Figure 2.6: Two bladeRF 2.0 xA9 clock synchronization block diagram [48]

2.2.2 SDR Development kit

The SDR development kit is a software platform in which DSP algorithms can be developed in coding or block diagram. Matlab/Simulink is a development software by MathWorks that is widely used in modelling model-based systems. With the Hardware support package in the communication/RF/wireless system toolbox, it can connect their system models with SDR platforms so that they can prototype, verify and test practical wireless systems [47].

Unlike LabView and GNU Radio, Matlab/Simulink is user-friendly. In addition, the rich function library provided by MATLAB can be called directly without repeated writing.

The BladeRF supports MATLAB and Simulink bindings of the C/C++, allowing using the SDR within these software packages. However, the blocks provided by Nuand don't support 2x2 MIMO. Jose. Amador [51] firstly test 2x2 MIMO in MATLAB/Simulink, but it only supports single BladeRF. Multiple BladeRFs synchronization is presented in section 2.4.2.

Nuand's libbladeRF is the official interface library for BladeRF in C/C++. Their site [52] describes the use of each module of the API, including some examples of boilerplate code. All libraries also show in function libbladeRF_ proto.m [53].

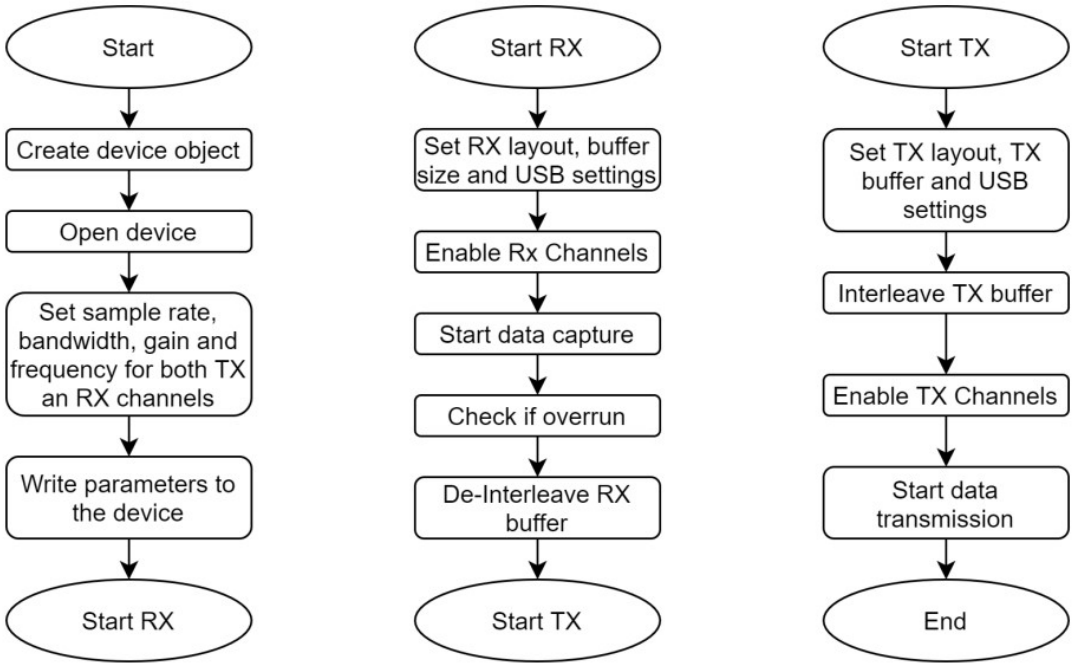

Figure 2.7: Device setup and utilisation [52]

2.2.3 Antenna selection

The carrier frequency determines the distance between elements as described by the equation 2.6

$$d \geq \frac{\lambda}{2} = \frac{c}{2f} \tag{2.6}$$

where d is the minimum distance between antennas, λ is the wavelength, c is the light speed. Thus, for 802.11ah standard ($f = 900MHz$), d equals 0.168m, and for 802.11ac standard ($f = 5.8GHz$), d is 0.026m. In order to unify the distance between antennas, the distance among all antennas sets to 0.168m.

Omnidirectional dipole terminal antennas working at 450MHz to 6GHz frequency bands were used for this thesis study. Dimensions of them are 218 * 58mm. The antenna has two setups, the straight position and the right angle (see), [54] indicates that the antenna gain of the two setups has no difference. This study uniformly adopted a straight position setup.

Two frequency bands antenna 3D gain pattern is depicted in Figure 2.9. The results show that the maximum antenna gain can reach about 0dB on the 5.8GHz frequency, the gain is lower in the direction of about 40° in elevation, 80° in azimuth and 60° in elevation, 50° in azimuth. For the 900MHz frequency band, the maximum antenna gain can reach about 5dB, gain is lower in the vertical direction.

Figure 2.8: Antenna setup, left is right position and right is straight position [54]

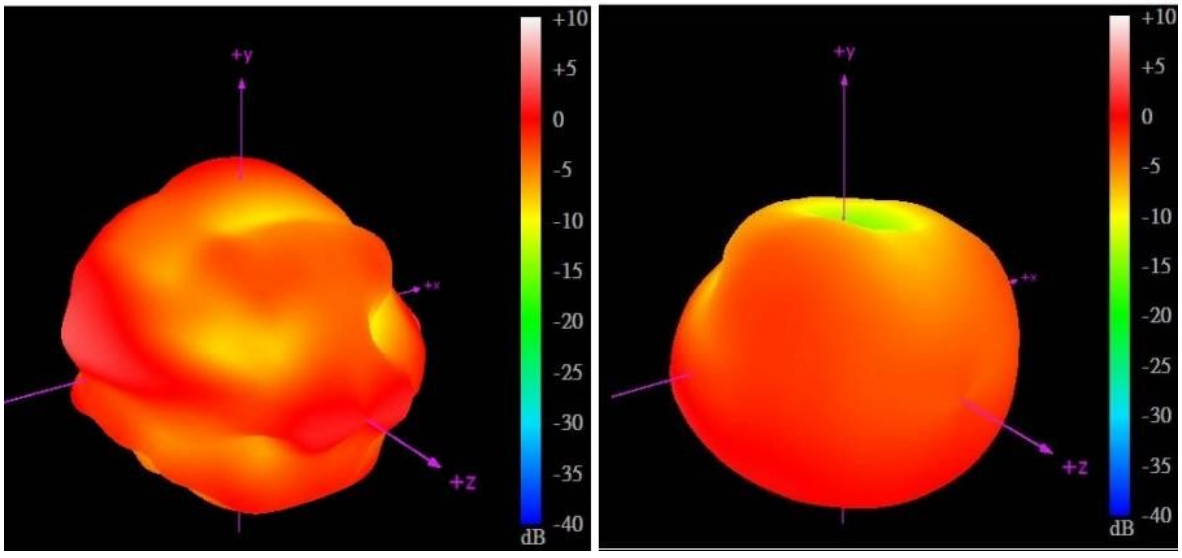

Figure 2.9: 3D radiation patterns(Straight position), from left to right, f is 5.8GHz to 900MHz [54]

Parameters	Value	
Frequency	5.8GHz	900MHz
FFT point N	64	64
# of OFDM symbols M	1024	1024
Subcarriers modulation m	4	4
# of pilots N_P	4	4
Pilots' locations P_L	Antenna 1 [34; 40; 46; 52]; Antenna 2 [37;43;49;55]	Antenna 1 [8; 15; 22; 29]; Antenna 2 [10;17;24;31]
Guard band N_{CP}	[6;5]	[6;5]

Table 2.2: 2x2 MIMO-OFDM frame specifications

2.3 OFDM frame specifications and structure

2.3.1 OFDM frame specifications

In this thesis, the purpose is to establish a double-band testbed JCAS hardware/software system using the MIMO-OFDM technique which collects CSI to identify human postures. Hence, we determine the specifications of the system by considering the requirements and SDR limitation and take the 802.11 ah/ac standard as a reference for double-band.

The specifications used in the system are shown in Table 2.2. As it's seen, both frequency band has the 2x2 MIMO configuration. The spectrum contains 64 SCs, including 4 pilots and 52 data in the payload. DC and higher/lower edge SCs (Cyclic Prefix (CP)) are empty to avoid the DC component in the OFDM waveform and eliminate inter-symbol and inter-carrier interference [1]. If all OFDM symbols use the same pilots, it would cause spectrum leakage(inter-spectral interference), that is the main spectral line produces many side lobes, causing interference between spectral lines. In order to prevent it, the pilot sequence is cyclically rotated over symbols and each antenna's pilot location is different. Signal bandwidth is limited to 2MHz due to BladeRF being locked to 2Mbps in RX for the MIMO scenario.

2.3.2 OFDM frame structure

Since both 802.11ah and 802.11ac protocols are used in this study, it is better to use a common frame structure for both protocols. The frame structure of our system shown in Figure2.10 is the universal frame structure of the 802.11 series. It consists of the preamble and payload. In the preamble part, it contains short and long preambles. The function of Short Training Field (STF) is coarse time, frequency synchronization and frame detection. Longer Training Field (LTF) is for fine symbol synchronization and channel estimation [1]. In the payload part, only data symbols exist. Additionally, CP is inserted to the left side of the symbol and LTF has an extra

guard interval in the beginning.

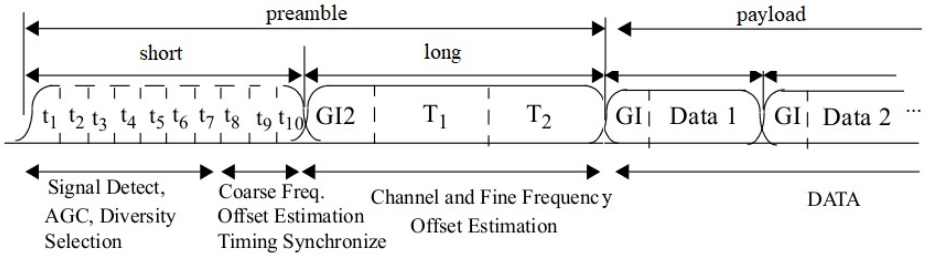

Figure 2.10: Testbed Frame Structure [12]

2.4 Transceiver Design

The design of the transceiver is done on Simulink, as shown in Figure2.11. A series of binary sequences are generated by the bit generator, SCs modulation is completed by baseband modulator, and then two channels' OFDM signals are obtained through Fast Fourier Transform (FFT) and multiplexing. After adding the preamble, the frame is generated and transmitted to the BladeRF TX end, which completes the work of the TX. As for RX, the BladeRF RX port receives OFDM frames through antennas. After time and frequency synchronization, the initial position of the frame is determined. And then, using algorithms to estimate the channel can obtain raw CSI.

2.4.1 Transmitter Design

Since the whole TX is composed of the Simulink blocks, this section only presents block parameter configurations. The actual simulation structure is shown in Figure2.12.

Bit Generator

Binary data is generated by Bernoulli Binary Generator [55], where sample time equals

$$T_{bit} = \frac{1}{2(N - N_{CP} - N_P * 2 - 1) \cdot \Delta f \cdot \log_2 m} \tag{2.7}$$

sample per frame is

$$BitFrm = M(N - N_{CP} - N_P * 2 - 1) \cdot \Delta f \cdot \log_2 m \tag{2.8}$$

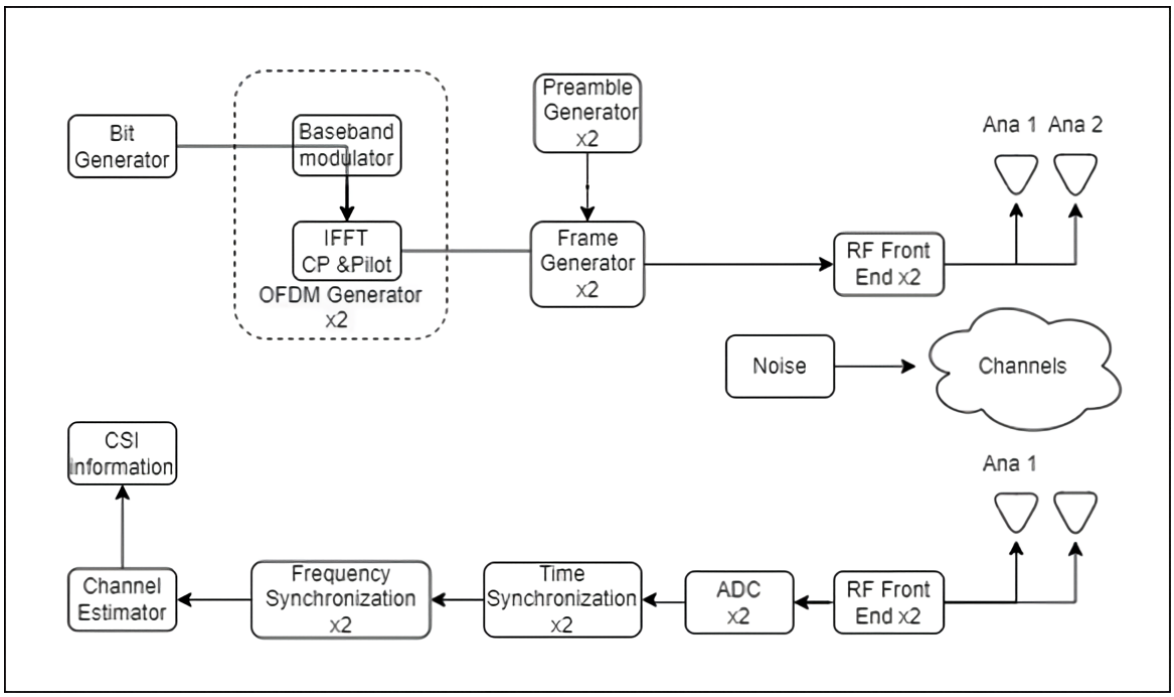

Figure 2.11: Transceiver block diagram

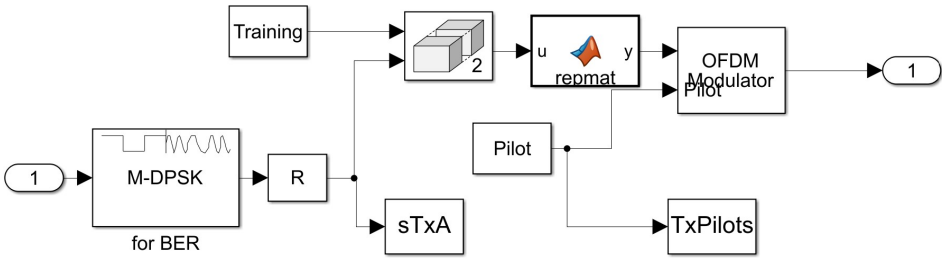

Figure 2.12: Transmitter Block in Simulink model

$N - N_{CP} - N_P * 2 - 1$ is the number of SCs filled in data, when $N = 64$, it's 52.

Preamble Generator

The STF and LTF are often used for synchronization, so their values are known for RX. A simple approach is to use a shift counter to generate a pseudorandom binary sequence. In this thesis, I used Pseudonoise (PN) Sequence [47] to generate preambles. PN Sequence uses a 7-bit shift counter, which is shown in Figure 2.13. STF symbol can be defined in the frequency domain as

$$STF(z) = \sqrt{\frac{13}{6}}(z^4 + z^3 + 1) \tag{2.9}$$

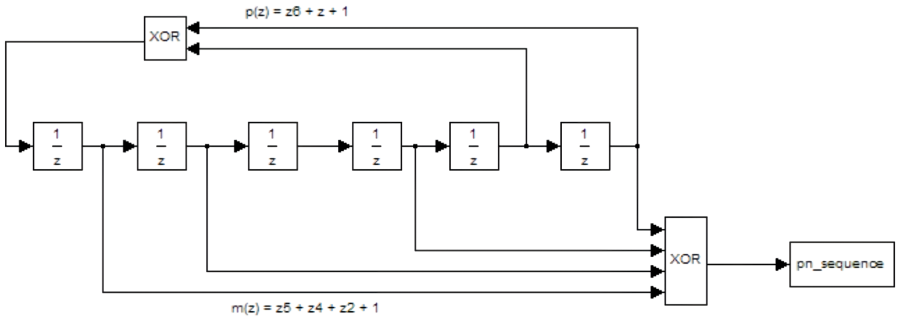

Figure 2.13: PN Sequence Generator [47]

And the initial state is [0 0 0 1 0 0 1]. And it's periodic. This characteristic will be useful for synchronization.

As for channel estimation, it will be performed by LTF symbols. Because we use the 2x2 MIMO scenario, the number of LTF symbols, which is determined by TRX antenna quantity, is two. And generator polynomial is

$$LPF(z) = z^7 + z^2 + 1 \tag{2.10}$$

The initial state is [0 0 0 0 0 1].

Baseband and OFDM modulation

As for the SC modulator and OFDM modulator, parameters are in Table 2.2. In order to further reduce the interference of adjacent frequency bands and make the transition between symbols smooth, the OFDM modulator sets a raised cosine window, and the size of the window is set to $\frac{N_{CP}}{2}$ [47].

Pilots are added to the OFDM modulator for residual phase offset correction [12], and channel estimation. Similarly, the PN sequence is also used on pilots (see Figure 2.13). The generator polynomial is

$$P(z) = z^7 + z^3 + 1 \tag{2.11}$$

And the initial state is $[111111]$.In this way, the OFDM frame is completed, Figure 2.14 shows the assembled frame in the 5.8GHz frequency band.

2.4.2 Receiver Design

CSI has measurement errors due to inherent flaws in WIFI devices. To extract CSI correctly, the premise is to receive the OFDM signal precisely and then compensate for potential amplitude and phase errors. The implementation of the RX block by

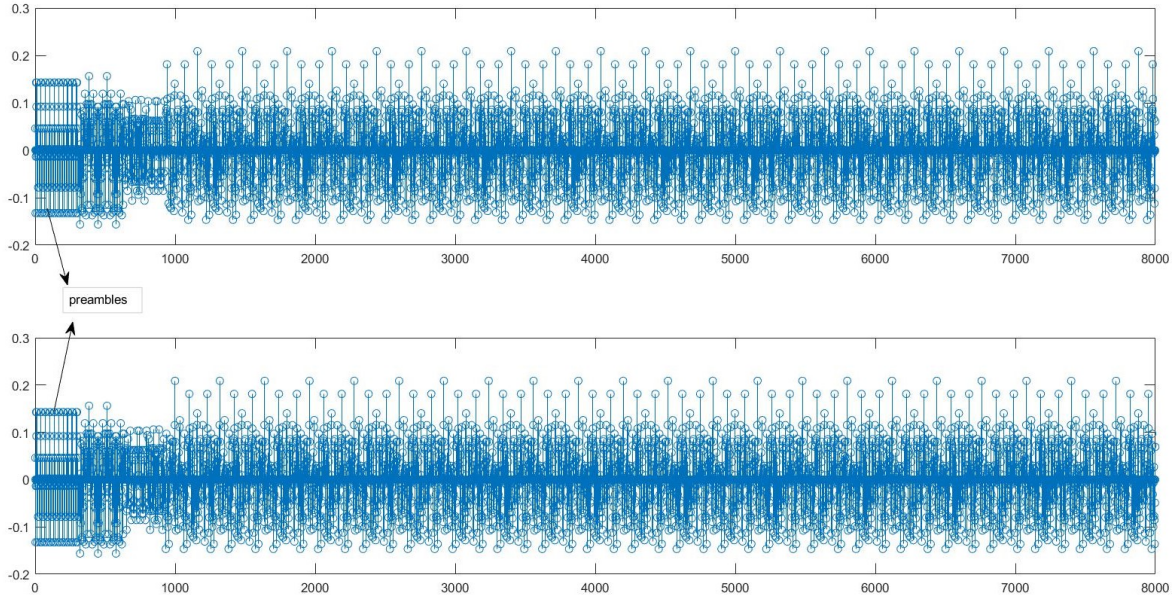

Figure 2.14: 5.8GHz Frame waveform in time domain

MATLAB/Simulink is in Figure2.15. The algorithms applied on RX are as follows

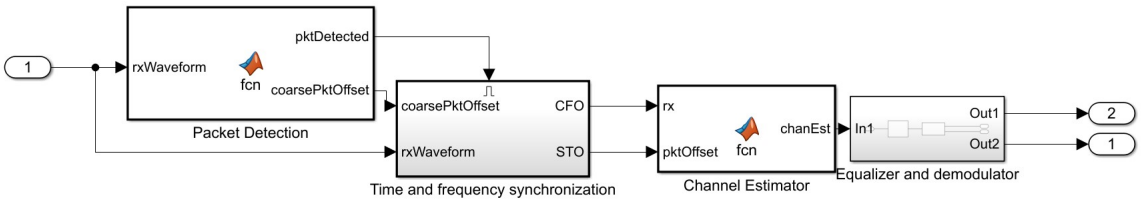

Figure 2.15: Receiver Block in Simulink model

Clock synchronization

Before starting software synchronization, two BladeRFs clock synchronization should finish. In theory, high-quality clock synchronization could solve coarse time/frequency synchronization. The device connection is shown in Figure 2.6.

In the schematic diagram of bladeRF [56], it indicates that 10MHz reference must provide 3.8V voltage on RFIN(J95 pin) to enable it. The connection only supports UF.L cable.

Results show that time and frequency are roughly synchronized in short distances(in near-field). However, in far-field (actual measured distance), time is out of synchronization. Thus, it's necessary to use algorithms to synchronize them.

Packet Detection

In RX, the first and most important step is to find the signal frame and perform time synchronization. There are various methods proposed to detect OFDM burst signal [1], [57], [58]. In this prototype, we adopted the cross-correlation algorithm. The short training sequence stored in the receiver in advance is cross-correlated with the received signal. And then, according to the calculated threshold, the outset of the frame is found. The 2x2 MIMO detected system model can be written as

$$C(n) = \sum_{i=0}^{2} \sum_{j=0}^{2} y_i[n] y_j[n+D]^* \tag{2.12}$$

$$P(n) = \sum_{i=0}^{2} \sum_{j=0}^{2} \mid y_j[n+D] \mid^2 \tag{2.13}$$

$$d(n) = \frac{\mid C(n) \mid^2}{(P(n))^2} \tag{2.14}$$

Where $y_i[n]$ is the i^{th} stream of received signal samples,$y_j[n+D]$ is the j^{th} transmitted STF symbol in the j receiving channel, where D is the length of the short preamble. Because STF repeats per 16 samples, $D = 16$ for this case. $d(n)$ is the decision metric. The decision is made by comparing it with a threshold.

Time synchronization

After computing the decision metric, the beginning of the packet is estimated for time synchronization. Since an OFDM frame has 10 consecutively repeated STFs, each received STF is correlated with the original STF sequence. When there is only one peak for each detection, it means that TX and RX are time-synchronized.

Algorithm 1 describes the process of finding the initial package.$\varsigma = \frac{\sqrt{P_{sym}}}{2}$ varies with symbol power P_{sym}. When the first sample that is higher than the threshold occurs, the cross-correlation value of this sample and the STF stored in the receiver is calculated. After repeating 10 times, if there is only one peak, then the frame is detected.

Figure 2.16 depicted the correlation between the TX and RX after time synchronization. Obviously, only one peak in the center means time synchronization successes.

Frequency synchronization

Due to the local oscillator difference between TX and RX, carrier frequency offset (CFO) problem exists, which causes the frequency shift in RX. After clock synchro-

while *scan detect packet* **do**
  initial;
  measure the P_{sym};
  update ς;
  while *count*≤ 10 **do**
    move to the next STF;
    correlation;
    if *one peak in the correlation* **then**
      count++;
    else
      break;
    end
  end
  if *count=10* **then**
    record packet initial location idx*, finish time synchronization;*
  else
end

Algorithm 1: Time detection and synchronization algorithm pseudo code [1]

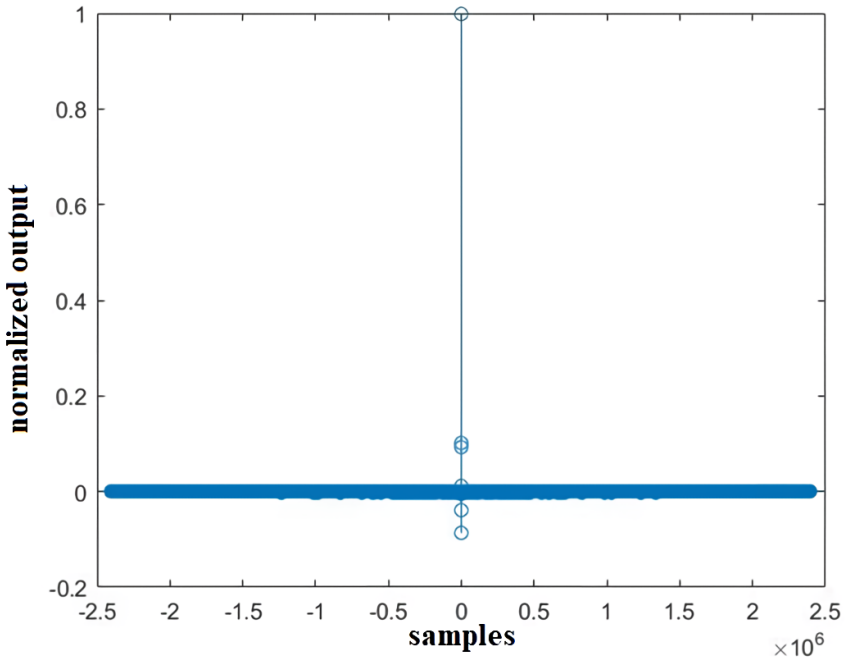

Figure 2.16: Correlation after time synchronization [1]

nization, two BladeRFs share the same 10 MHz reference clock, the central frequency is synchronized. However, there are still carries residual errors, leading to a phase shift around pi in the 5.8GHz frequency band [12]. While the maximum body movement phase shift is 0.5π in general, it's ambiguous to identify the phase/frequency offset source [21].

For enhancing the communication quality of the prototype, it is still necessary to synchronize frequency in the software. There are already various algorithms applied on both time and frequency domains [1], [12], [57], [59]. Figure2.17 indicates that the pilots-long-preamble-based method has lower BER. Hence, the research chooses the Moose+ Classen method. Two LTFs are repeated per 64 samples ($L = 64$)in this

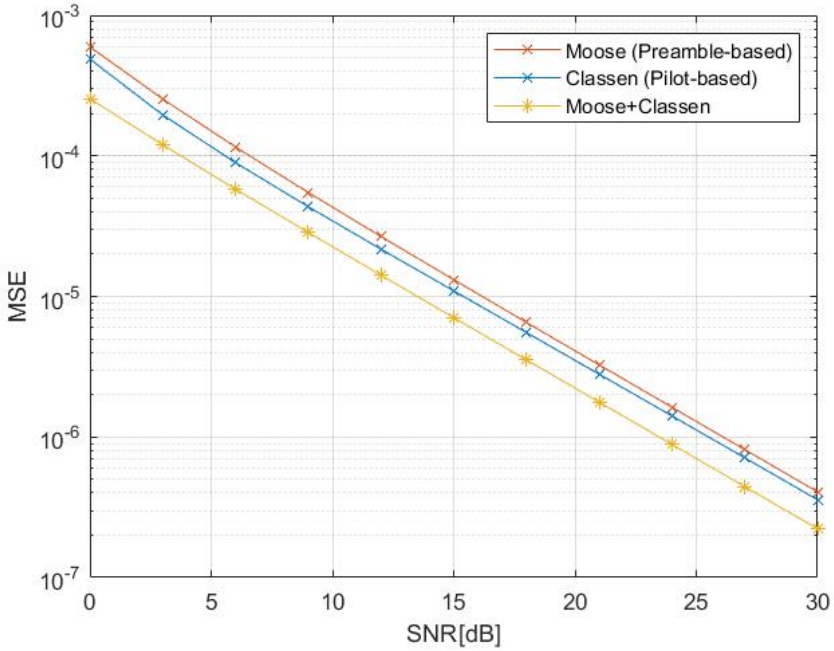

Figure 2.17: Comparison of three frequency synchronization algorithms

testbed, which can be used for fine frequency estimation in the time domain. For the MIMO scenario, the model can be written as [1]

$$\begin{aligned} y_i[n] &= x_i[n] \cdot e^{j2\pi f_{TX} n T_s} \cdot e^{-j2\pi f_{RX} n T_s} \\ &= x_i[n] \cdot e^{j2\pi (f_{TX} - f_{RX}) n T_s} \\ &= x_i[n] \cdot e^{j2\pi \Delta f_d n T_s} \end{aligned} \tag{2.15}$$

where $x_i[n]$ is the i_{th} OFDM symbol in a TX packet, T_s is the sampling rate of system, f_{Tx} and f_{RX} are TX and RX carrier frequency separately, Δf_d is the CFO between TX and RX carrier frequency. The phase offset among 10 consecutive STFs can be

used in the algorithm to calculate the CFO.

$$\begin{aligned}\phi_{LTF} &= \sum_{n=0}^{L-1}\sum_{i=0}^{2}\sum_{j=0}^{2} y_i[n]y_j[n+D_L]^* \\ &= \sum_{n=0}^{L-1}\sum_{i=0}^{2}\sum_{j=0}^{2} x_i(n)e^{j2\pi\Delta f_d nT_s}(x_j(n+D_L)e^{j2\pi\Delta f_d(n+D_L)T_s})^* \\ &= e^{j2\pi\Delta f_d D_L T_s *}\sum_{n=0}^{L-1}\sum_{i=0}^{2}\sum_{j=0}^{2} \mid x_i(n)x_j(n+D_L) \mid^2\end{aligned} \tag{2.16}$$

where $y_j[n+D_L]^*$ is the j^{th} received antenna LTF symbol, here $D_L = 64$, which is similar to Equation2.12. Thus the CFO can be calculated by

$$\Delta f_d = -\frac{1}{2\pi D_L T_s} arg(\phi_{LTF}) \tag{2.17}$$

After using Δf_d to compensate for the frequency difference between TX and RX, then using pilots for more precise frequency synchronization. The formula can be expressed as

$$\Delta f_p = -\frac{1}{2\pi P(N+L)T_s} arg(\sum_{n=0}^{L-P}\sum_{k}\sum_{i=0}^{2} y_{n+P,i}[n]y_{n,i}[k]^* x_{n,i}[k]^* x_{n+P,i}[n]) \tag{2.18}$$

where $x_{n,i}[n]$ is the pilot symbol saved in RX and P is the delay parameter which is determined by the pilots' location. So far the frequency synchronization is completed.

Channel Estimation

The common approach to performing channel estimation is by Maximum Likelihood (ML) estimator. It can be used for each SC of LTF in frequency domain [12]. The 2x2 MIMO-OFDM prototype in the time domain is [1]

$$y[n] = h[n]x[n] + n_w \tag{2.19}$$

$$h[n] = \begin{bmatrix} h11 & h12 \\ h21 & h22 \end{bmatrix} \tag{2.20}$$

where $h[n]$ is the 2x2 channel matrix, N_w is the $i.i.d$ Gaussian white noise. In the frequency domain, it could be

$$Y[k] = H[k]X[k] + N_w, k = 1, 2, ...N \tag{2.21}$$

k represents SC, thus $H[K]$ is the channel matrix of the k_{th} SC, it can be written as

$$H_{i,j}[k] = \frac{[Y_{j,1}[k], Y_{j,2}[k]]y_i^*[k + D_L]^T}{2x_i^*[k + D_L]} \tag{2.22}$$

where $Y_{j,1}[k]$ is the first LTF symbol of the j_{th} received channel of the k_{th} SC,$y_j^*[k + D_L]$ is the j_{th} received antenna LTF symbol of the k_{th} SC,$x_i^*[k + D_L]$ is LTF symbol of the k_{th} SC of the i_{th} transmitted channel .D_L is define in equation 2.10.

Since the signal band is narrow (see Table 2.2) and has high SNR(see section2.5.1), it's unnecessary to consider noise reduction.

MIMO Equalizer

In the MIMO-OFDM system,Inter Carrier Interference (ICI) problem is solved after good frequency synchronization. However, each receive antenna includes the signals transmitted by all transmit antennas, so it is necessary to classify and identify signals from different sources at RX, especially for systems that transmit simultaneously on dual bands. Thus, using a MIMO equalizer to remove spatial interference is indispensable.

Considering the high noise sensitivity of CSI. Mean Square Error (MSE) Equalizer is used in the implementation. MSE equalizer filter is to minimize $\mid X_{est}[k] - X[k] \mid^2$, that is [1]

$$W[k] = \frac{H[k]^H}{(H[k]^H H[k] + \sigma_N^2 I)} \tag{2.23}$$

where $W[k]$ is the pseudo-inverse of $H[k]$,σ_N^2 is the noise variance. It can be measured by [60].

Phase Offset Estimation

As mentioned in the section2.2.1, TXs and RXs are on separate BladeRF, the multipath effect and BladeRFs difference cause phase offset. Although clock synchronization and channel equalization correct the large phase error, still exists the phase offset on the symbol that affects the CSI's quality. This testbed uses pilot symbols to estimate residential phase offset, the equation is [1]

$$M[k] = X[k]e^{j\phi pilot} + n_w \tag{2.24}$$

where $\phi pilot$ is fixed phase offset on each symbol, k is the index of SC, the phase offset can be expressed as

$$\phi pilot = arg(\sum_{p=1} \sum_{k}^{P_L} M_p[k] X_p^*[k]) \tag{2.25}$$

where $M_p[k]$ is the p_{th} pilot in the k_{th} SC in estimation and $X_p[k]$ is transmitted p_{th} pilot in the k_{th} SC.

After multiplying the conjugate of it, the $\phi pilot$ is removed. And the compensated signal is

$$S[k] = M[k] e^{-j\phi pilot} + n_w \tag{2.26}$$

Baseband and OFDM demodulation

Similar to SC and OFDM modulators, the testbed uses Simulink Baseband and OFDM demodulator. Related parameters are in Table 2.2. These blocks work on validating the perfectly recover from RX to TX, which could provide convincing CSI.

2.5 Prototype Validation

In this section, we initially run the double-band communication interference test to eliminate the noise coming from the other frequency band. Secondly, it gives the equation of the free space link budget and the real TX power level. Thirdly, RX demodulator performance analysis is displayed. Thus the communication performance of the transceiver is proven. At last, the whole testbed validation is presented.

2.5.1 Single link interference test

Before implementing a concurrent double-band test, it must ensure there is no interference between two frequency bands. Thus, the test can set $f_{tx} = 5.8GHz, f_{RX} = 900MHz$ and vice verse. If there is no distortion (like sidelobe interference from adjacent channels) in the RX spectrum, it means there is no interference running on two frequency bands simultaneously. The testing model in Simulink is shown in Figure2.18, where the transmitted signal is selected as QPSK and both channels set $-0.5MHz$ and $-0.25MHz$ phase offset separately. Figure2.19 indicates that double-frequency band communication has no interference because of no distortion in the RX spectrum of the other frequency band.

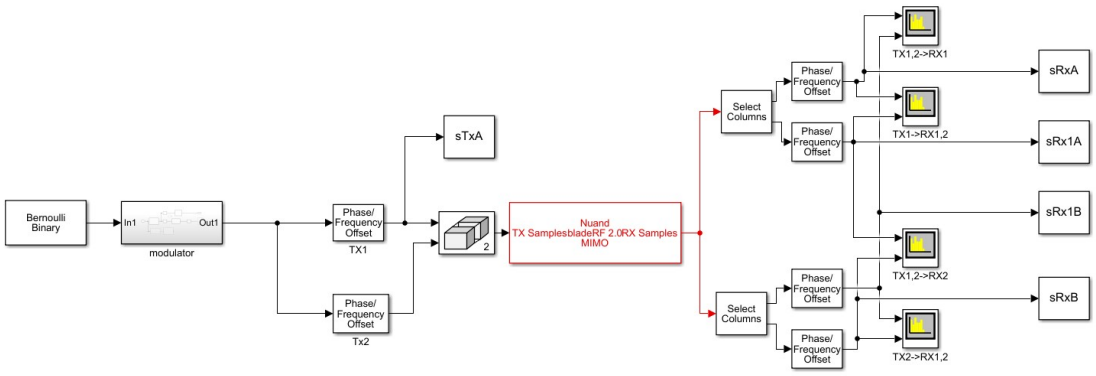

Figure 2.18: Simulation model for testing single link interference

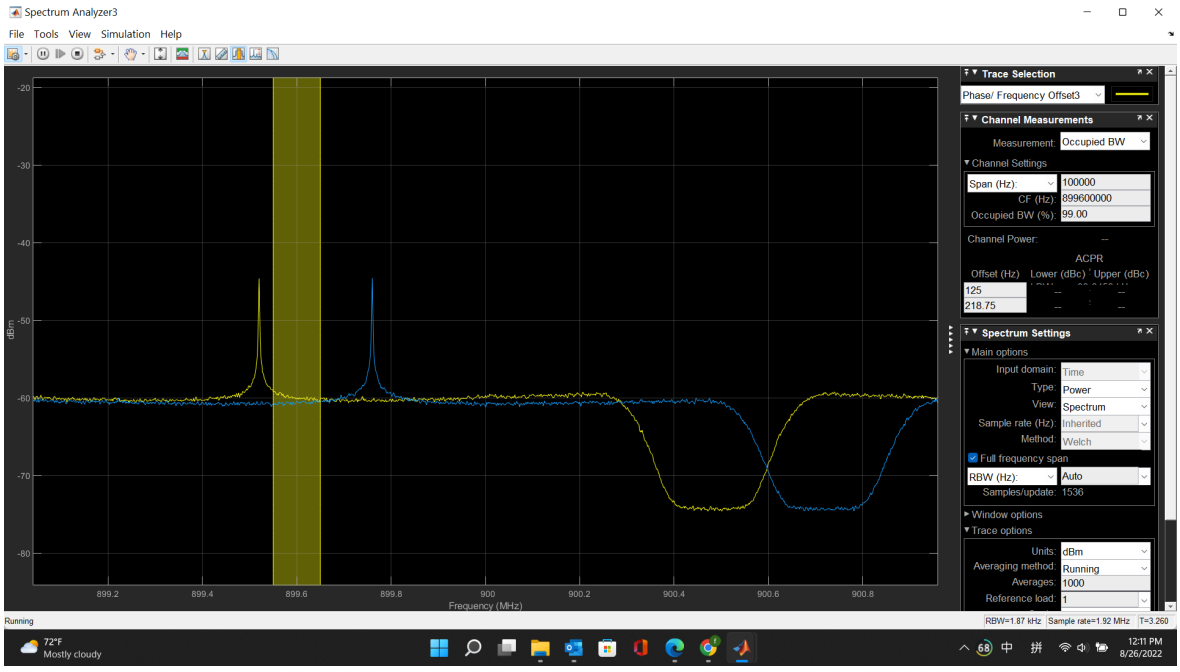

Figure 2.19: $f_{tx} = 5.8GHz, f_{RX} = 900MHz$ Receiver spectrum

2.5.2 Link budget

According to Friis' law [12], received power can be described as

$$P_{RX}(d) = \frac{G_{TX}G_{RX}}{L_f(d)}P_{TX} = P_{TX}(\frac{\lambda}{4\pi d})^2 G_{TX}G_{RX} \tag{2.27}$$

where $\lambda = \frac{c}{f}$, d is the distance between TX and RX, L_f is the free space path loss and G_{TX}, G_{RX} are the gain of TX and RX respectively. Rewrite the equation in dB,

$$P_{RX|dB}(d) == P_{TX|dB} + G_{TX|dB} + +G_{RX|dB} - 20\log_{10}(\frac{4\pi d}{\lambda}) \tag{2.28}$$

In order to measure the TX power level of bladeRF, the SMC cable is used to connect BladeRF TX and Spectrum Analyzer. The $P_{TX|dB} + G_{TX|dB}$ in this testbed is around -40dB, see Figure2.20.

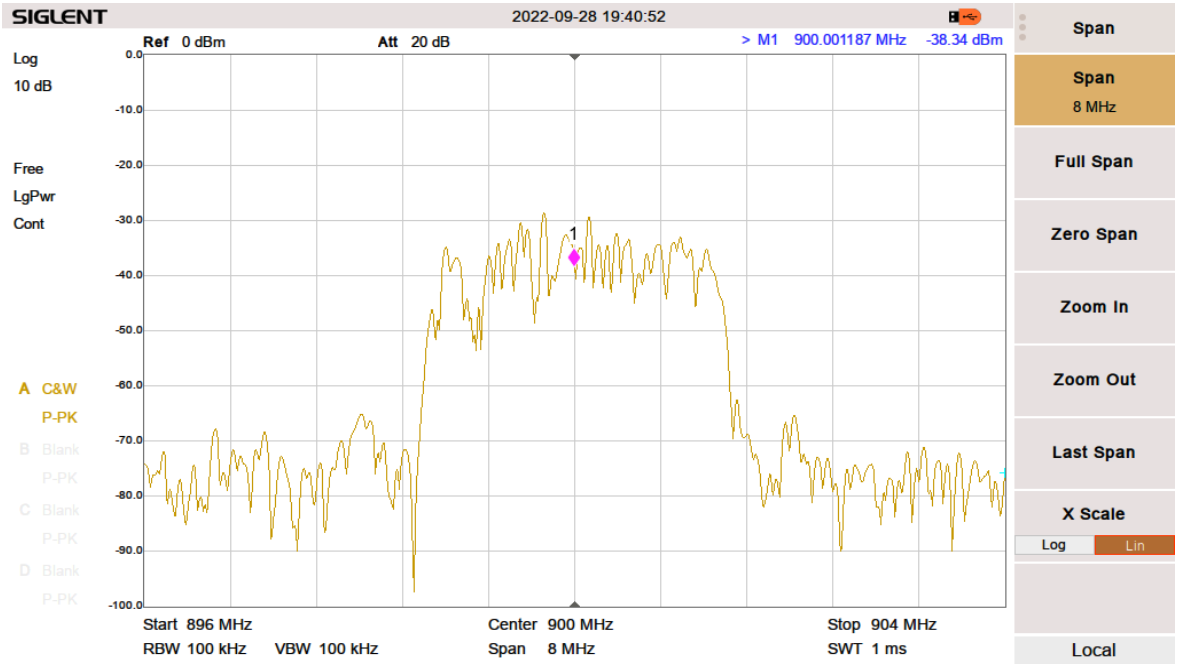

Figure 2.20: Received TX power in Spectrum Analyzer with 60dB Gain in BladeRF

2.5.3 RX performance test

BER is the ratio of error bits and overall transmitted bits. Its performance determines the ability of RX synchronization and noise reduction, which can intuitively reflect the communication capability of the transceiver. Before implementing the real setup, the test only contains the modulator and demodulator adding noise and phase error. The simulink model is shown in Figure2.21, TX1 and TX2 set $\frac{\pi}{2}$ and π phase offset respectively. The former is the general human activities phase offset and the latter is the maximum phase offset the demodulator could compensate.

According to the equation 2.27, the path loss is inversely proportional to the square of the distance. It determines the received power level. Hence, the 5.8GHz signal has lower RX power and SNR than a 900MHz signal in the same scenario. Thus, we use the 5.8GHz signal as an example.

In order to evaluate the performance of the receiver, we added four types of phase and noise values. Table2.3 shows steady-state BER and configuration in the RX performance test, where the simulation time is 15s. Figure **??** a concludes a larger phase shift in the transmitted symbols results in a more extensive steady-state transient time for the carrier(frequency and phase) synchronisation. In the worse

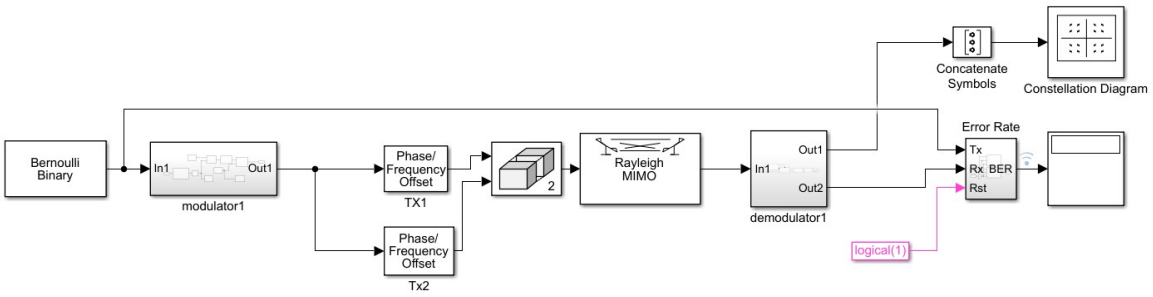

Figure 2.21: Simulink model for testing the Modulator and Receiver blocks

Experiment Number	SNR/dB	ϕ	BER
Baseline	40	0	0
EX1	10	$\frac{\pi}{2}$	2.59e-2
EX2	10	π	2.79e-2
EX3	20	$\frac{\pi}{2}$	2.98e-4
EX4	20	π	8.44e-4

Table 2.3: Results of RX simulation test

scenario($EX2$), BER performance is still acceptable, which means RX performance satisfies the requirements of extracting CSI.

2.5.4 Testbed performance test

In order to test the overall sensing performance of the prototype, including amplitude and Doppler shift in the time/frequency domain, a double-wire pendulum is introduced. As the frequency of pendulum can be calculated by formula2.29 [61]

$$f_{ball} = \frac{1}{T} = \frac{1}{2\pi\sqrt{\frac{I}{mgD}}} (\theta > 15^{\circ}) \tag{2.29}$$

where θ is the angle between the highest point and lowest point,T is the pendulum period,m is the ball weight, D is the distance from the center of mass to the point of suspension,I is the moment of inertia. For hollow metal ball,$I = \frac{2}{5}m\sqrt{D}$. The velocity of the pendulum is $v_{ball} = \sqrt{2gDsin\theta}$ The ideal model of the two-wire pendulum is shown in Figure 2.22. Because the larger the θ and m, the larger the pendulum frequency. Based on Table 3.1, $\theta = 30^{\circ}$,$m = 0.01kg$, $D = 90cm$. Thus $f_{ball} = 0.8307Hz$,$v_{ball} = 2.182m/s$. When $f_s = 5.8GHz$, Doppler shift $\Delta f_{Doppler} = 84.3707Hz$. When $f_s = 900MHz$, Doppler shift $\Delta f_{Doppler} = 13.0920Hz$. It means only the 5.8GHz frequency band could observe the Doppler shift.

To start the validation, we measure the static scenario that the ball is motionless. The setup of the experiment is shown in Figure 2.28. We can see the ball is in the

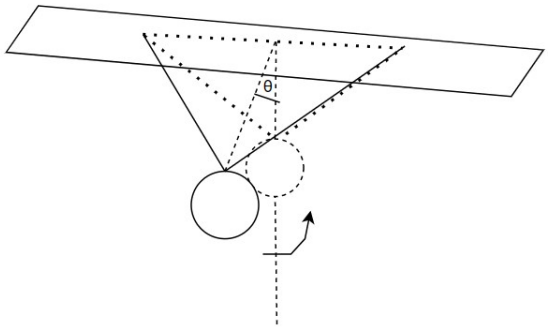

Figure 2.22: Two-wire pendulum structure

center between the left-side(orthogonal table) and right-side(parallel table)antennas. The string is tied to the scaffolds on the front and rear sides of the desk and placed in parallel, and the ball is fixed in the middle by the suction cup on the string. Before measuring, the ball is held with hands and fixed at a position with a 30-degree angle to the center. When the SDR platform was running, the ball is released.

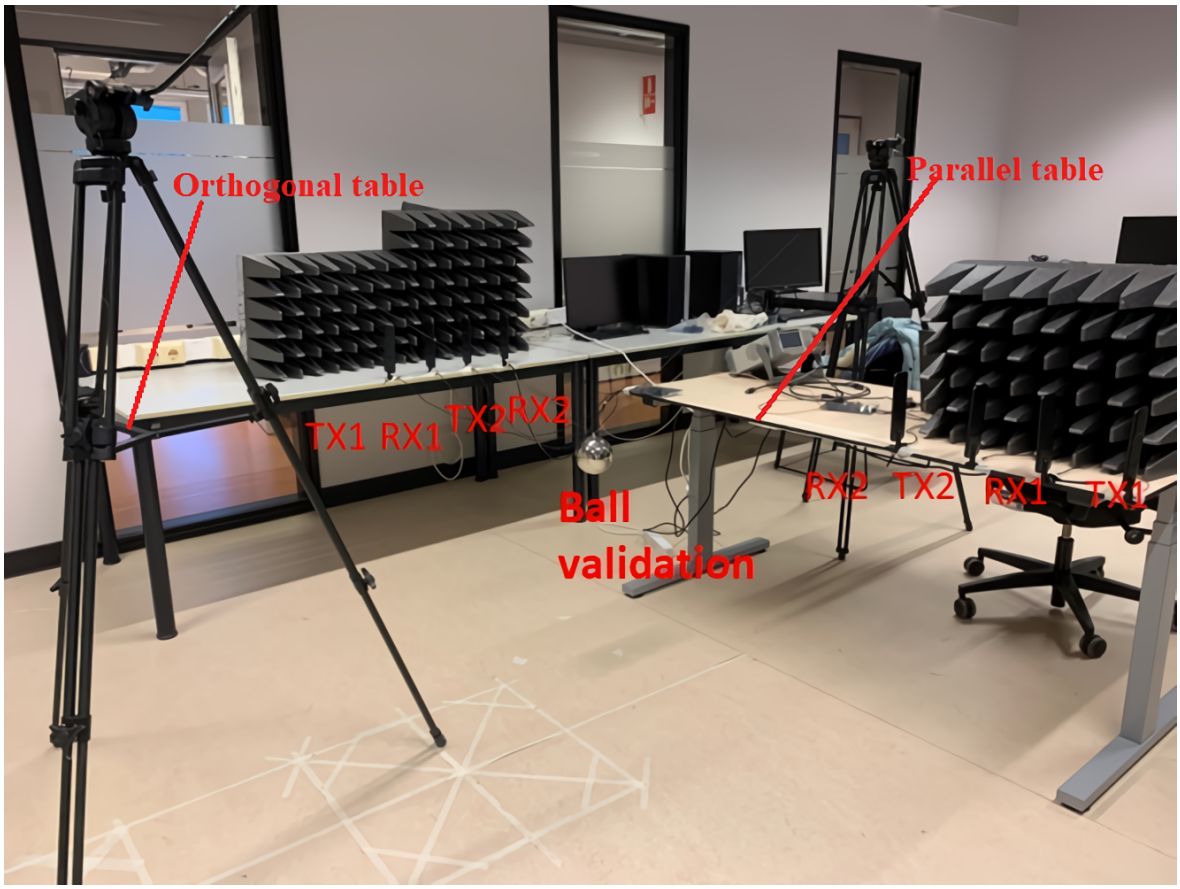

Figure 2.23: Static pendulum layout in orthogonal scenario

In this scenario, TX antennas on the orthogonal table operate on the 5.8GHz

frequency band. While TX antennas transmit 900MHz signal on the parallel table. Equivalently, orthogonal table antennas receive a 5.8GHz signal and parallel table antennas receive a 900MHz signal. In this scenario, the antenna RX2 on the left is on the same horizontal line as the antenna RX2 on the right and the distance between them is 2.4m. The 4 antennas on the left maintain a half-wavelength at 900MHz frequency (see section2.2.3), which is 16.8cm. The right 4 antennas have the same configurations. Thus the link budget among antennas could be calculated by equation2.28.

The prototype design in Simulink platform is in Figure 2.26, where the modulator block is shown in Figure 2.12, demodulator block use section 2.4.2 algorithms implement by MATLAB code (Figure 2.15). Due to the same blocks utilisation in two frequency band, the prototype only shows one of them.

Results for the static scenario are shown in Figure 2.24 with 900MHz carrier frequency, Figure 2.25 with 5.8GHz carrier frequency at 1.25Mbps sampling rate. The whole snapshot describes the process of signal processing and recovery(that is the first second block diagram of Figure 2.1 and the RX part in Figure 2.11). It starts with extracting IQ samples(the second figure) from the raw signals (the first figure) and then presenting the distribution of signal frequency components. After locating the initial location of the data packet, the algorithms(see section 2.4.2 and 1.1.3) supplement the frequency/phase offset. Later, the time/frequency domain information is extracted. Finally, the binary data could be demodulated after MIMO equalization.

The following conclusion can be drawn from Figure 2.24 and Figure 2.25.

(1) In static scenarios, both 900MHz and 5.8GHz carrier frequencies have good communication performance that all bits could be received correctly.

(2) 5.8GHz frequency has around 20dB path loss more than 900MHz frequency, which means the 5.8GHz frequency band has higher attenuation.

(3) 5.8GHz signals are more sensitive to channel fluctuation than 900MHz signals.

(4) Channel variation can be identified via Delay/Doppler spread.

According to the above conclusions, we record the Doppler shift of each OFDM symbol at the 5.8GHz frequency band and the 21st SC in each OFDM symbol amplitude to describe the double-wired pendulum motion at a 560kps sampling rate. Figure 2.27 indicates the frequency and Doppler shift of all OFDM symbols during the simulation time. Only when the metal ball has a non-perpendicular motion relative to the RX antenna, the OFDM symbol will produce a Doppler frequency shift. In equation 2.29, the theoretical maximum Doppler shift is 84.3707 Hz. But Figure 2.27 shows

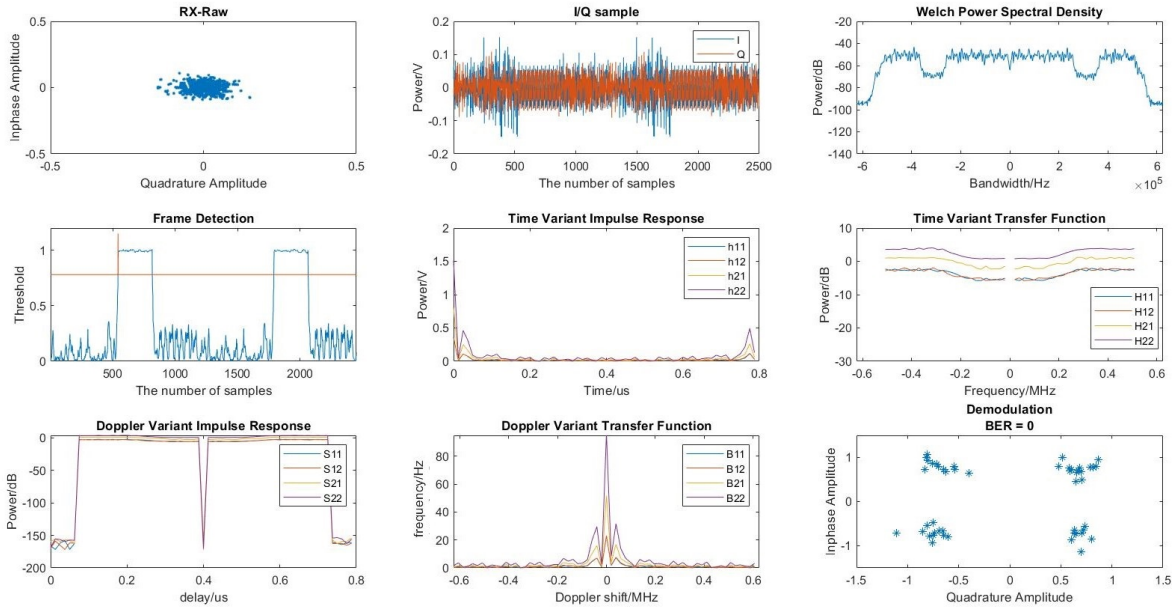

Figure 2.24: A snapshot of 900MHz 2x2 MIMO-OFDM Static channel scenario from the testbed channel analysis

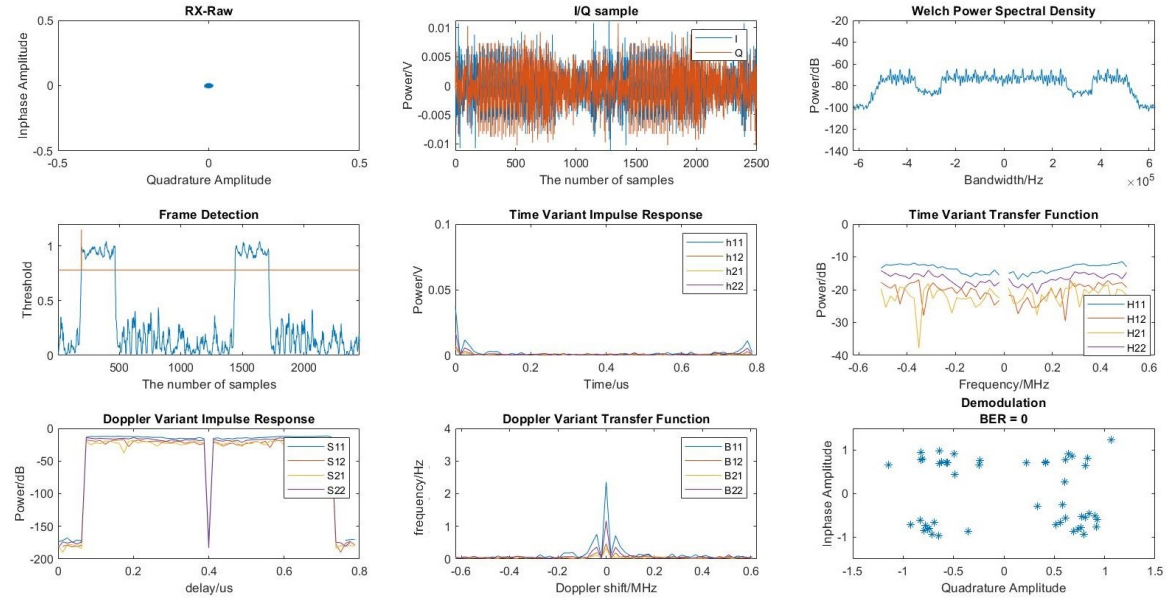

Figure 2.25: A snapshot of 5.8GHz 2x2 MIMO-OFDM Static channel scenario from the testbed channel analysis

that all TX/RX pairs have the same maximum Doppler shift at 70Hz, which is small than the theoretical value.

The reason why theoretical and real value is mismatched is that the actual speed

is smaller than the theoretical speed. As time goes on, the ball's moving speed decreases. And because the measurement uses an omnidirectional antenna, the angle between the ball and RX antennas is a series of values rather than a fixed angle. Moreover, the difference among the angle in different RX-ball pairs is far smaller than the Doppler resolution Δf_D. But the angle between the ball and the antenna reflects the amplitude fluctuation, which is embodied in the large difference in the peak power level. It is based on the fact that objects moving perpendicular to the direction of the receiver do not produce a Doppler shift, that is $cos\theta = 0$. In this scenario, the central power level of Doppler variant transform function $B_{i,j}$ satisfies $B_{11} > B_{22} > B_{12} > B_{21}$ compatible with the lab antenna layout.

Figure 2.28 presents the $21st$ SC amplitude for 500 OFDM signal. Thus, there is a total of $500 \times 1024 = 512000$ symbol. Unlike the amplitude in the Doppler spectrum, the power level of each SC depends on the distance between TX and RX antenna. The longer distance, the lower the power level. Thus, $h_{22} > h_{21} > h_{12} > h_{11}$ which fits the antenna setup. Owning to the ball locates in the center between RX1 and TX2 antenna on the orthogonal table, the fluctuation amplitude of h_{21} is the most obvious due to the smallest angle between the ball and RX antenna. However, the volume of the ball is not big enough to see the high amplitude variation. That's why the amplitude information is not clear.

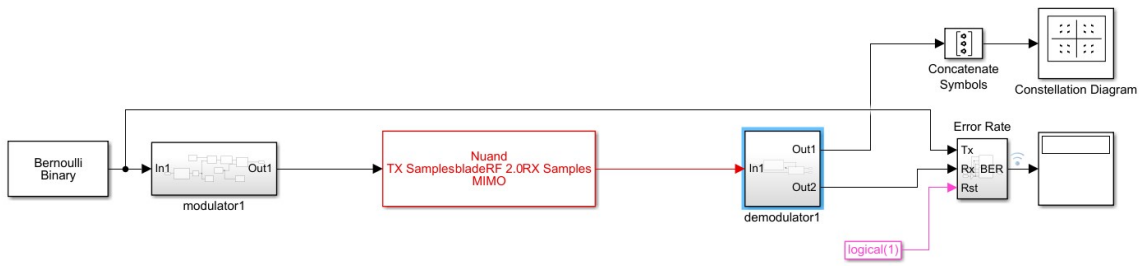

Figure 2.26: Transceiver Prototype Design in Simulink

Based on the above analysis, the testbed performance is performed, and then the human activities scenarios would introduce.

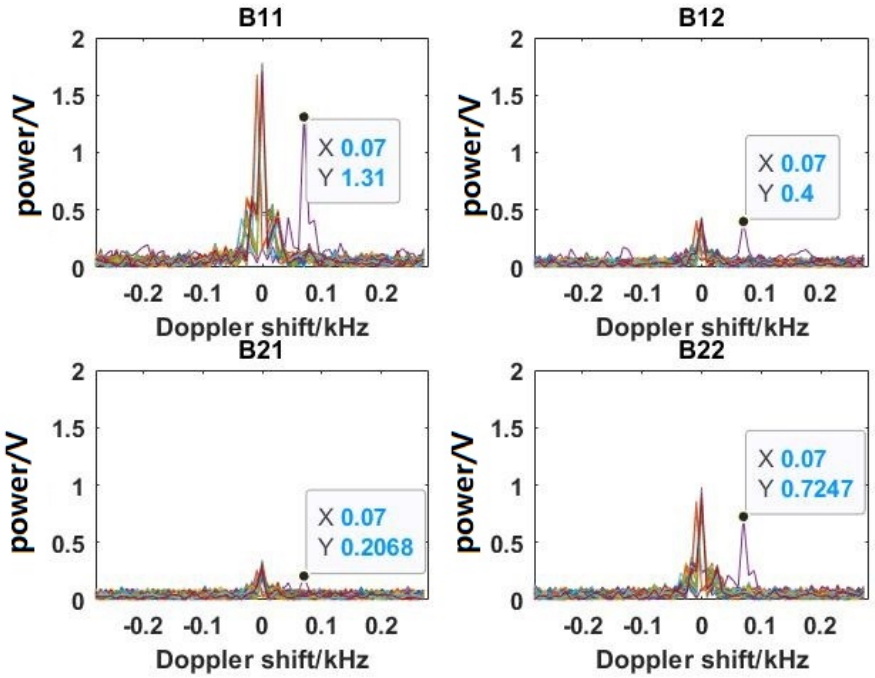

Figure 2.27: Doppler Variant Transfer Function of double-wired pendulum movement in orthogonal scenario

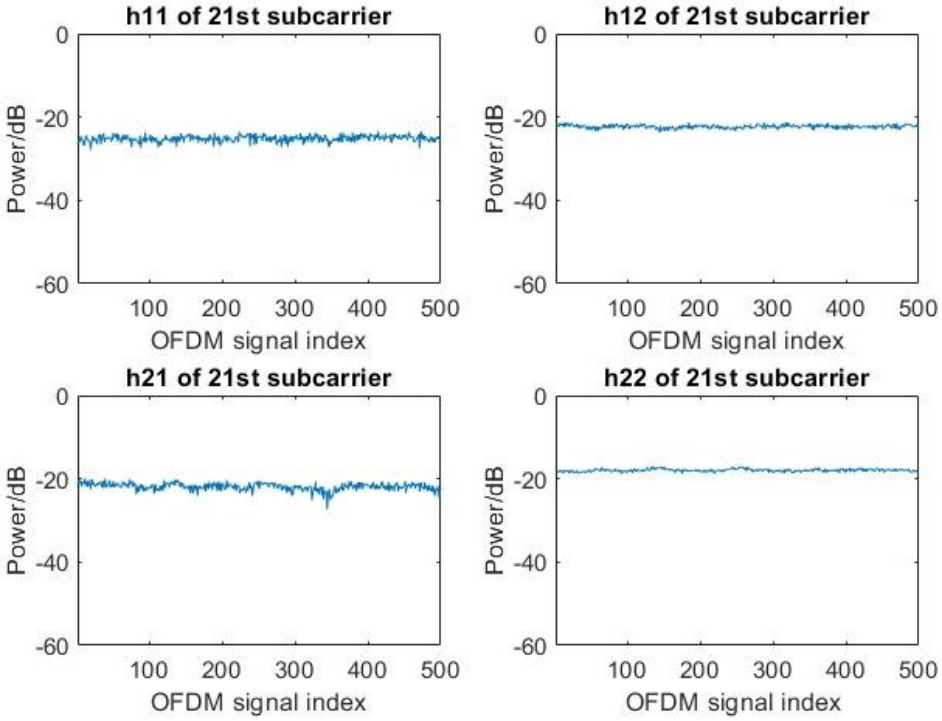

Figure 2.28: Time Variant Impulse Response of 21st subcarrier of double-wired pendulum movement in orthogonal scenario

Chapter 3

Measurement Campaign

This chapter presents the testbed study. With the testbed, the concurrent double-band MIMO-OFDM implement parallel and orthogonal scenarios with three different human activities. The testbed setup and real experiment validation are in section 3.1. Human activities raw CSI collection in two layouts are in section 3.2.

3.1 Testbed Setup

BladeRF stream configuration is in Table 3.2. The selection of parameter values reference [52] so as to no timeouts or dropped data. The relationship must be upheld for a given sample rate to

$$F_s > \frac{N_{trans}}{T_{stream}} \times N_{buffer} \tag{3.1}$$

Since the distance resolution is inversely proportional to the bandwidth, the localization of the indoor environment requires at least a meter-level resolution. However, due to the available band limitation of BladeRF in MATLAB/Simulink platform (see section 2.3.2), the minimum distance resolution can only reach 75m(see Table 3.1). That's why the thesis doesn't consider human localization. General human activities velocity is around $1 - 4m/s$ [11]. According to equation 2.4, the Δf_D in 900MHz should be $6 - 24Hz$,for 5.8GHz should be $38.67 - 154.66Hz$. In order to distinguish human activities, the specifications of double-band OFDM radar are set as Table 3.1. Theoretically, for general human activities, large body movement is visible in the Doppler domain.

Subcarrier spacing Δf	31.25kHz	19.531kHz	8.75kHz
Sampling rate(Bandwith) $F_s = BW = N \cdot \Delta f$	2Msps	1.25Msps	560ksps
Transmit OFDM symbol duration $T_{sym} = \frac{1}{\Delta f}$	0.032ms	0.0512ms	0.114ms
Range resolution $\Delta r = \frac{c}{2BW}$	75m	120m	267.8571m
Doppler resolution $\Delta f_D = \frac{1}{MT_{sym}}$	30.52 Hz	19.07 Hz	8.54Hz
Maximum unambiguous range $r_{max} = \frac{c}{2\Delta f}$	4800m	7680.1m	17143m
Maximum unambiguous Doppler $f_D(max) = \pm\frac{1}{2T_{sym}}$	15.625kHz	9.7655kHz	4.375kHz

Table 3.1: OFDM radar specifications of three sampling rates

Frequency	5.8GHz	900MHz
TX Gain G_{TX}	60dB	60dB
RX Gain G_{RX}	25dB	25dB
# of buffer N_{buffer}	64	256
# of USB transforms N_{usb}	8	4
stream buffer sizeN_{trans}	1024*22	1024*20
stream timeout T_{stream}	5000	1000

Table 3.2: BladRF configuration in double-band

3.2 Measurement Scenarios

In this section, I measure the squat, jumping jacks and circling in parallel and orthogonal antenna layouts. Concurrent double-band 2x2 MIMO-OFDM communication and sensing are in the same SDR platform. For all test cases, the simulation time is 5s. Thus, there are 500 OFDM signals transmitted with 900MHz carrier frequency. And 20 OFDM signals transmitted with 5.8GHz carrier frequency. Each scenario event tests 20 times. There are total $20 \times 3 \times 2 = 120times$ measurements.

3.2.1 Scenarios

Because the angle of the RX antenna and object has a significant effect on Doppler shift and amplitude. Thus, the experiment provides two kinds of relative locations between RX and TX antennas, they are parallel and orthogonal layouts. The view of both scenarios is in Figure 3.1, 3.2. The orthogonal scenario is the same as the double-wired pendulum layout. And the parallel scenario, the left side and right side antennas are in total alignment, namely, $TX1(left) - TX1(right), TX2(left) - TX2(right), RX1(left) - RX1(right), RX2(left) - RX2(right)$ are on the same horizon.

Besides, absorbing foam is deployed around the antennas to reduce the direct reflection from the wall. The floor plan of the lab environment and sketch of the object location is in Figure3.3. It shows the vertical distance between objects and antennas. Obviously, the location of the object could block most of the free space

Figure 3.1: Orthogonal Antenna scenario

Figure 3.2: Parallel Antenna scenario

transmission which ensures the signal transmission via the human body reflection.

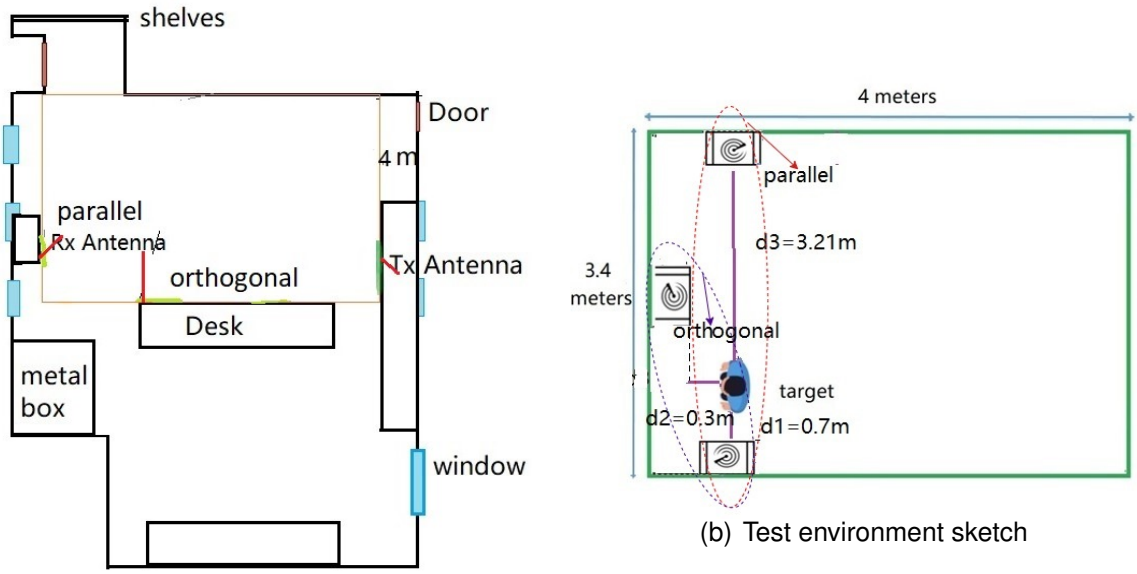

(a) Lab floor plan

(b) Test environment sketch

Figure 3.3: The plan of lab environment

3.2.2 Human Activities Analysis

Due to the indoor environment (short distance), the movement of the human body cannot be regarded as a point movement, that is, the movement of each part of the human body has a corresponding Doppler shift and amplitude fluctuation. Thus, each event can be split into a series of combinations of different parts of the movement.

Section3.1 mentioned that human activities velocity is around $1 - 4m/s$ and the Doppler shift is $6 - 24Hz$ at 900MHz. Because the relative speed of the object and RX is proportional to the Doppler shift (see equation 2.4). The low-speed movement is difficult to observe due to the low Doppler shift being smaller than the Doppler resolution(see table 3.1). To solve this problem, we choose three violent sports as matching events that have large differences in speed, direction and relative angle from RX to the body. In that case, amplitude and Doppler shift could distinguish these events. The three events sketch is shown in Figure, from left to right, the exercise is squatting, jumping jacks and circling around.

Squatting can be roughly broken down into two processes: squatting down and up. Since the jumping and squatting process of the human body is similar to the free fall motion [62], it can be calculated by a uniformly accelerated motion equation,

$$v = \sqrt{2gh} \tag{3.2}$$

where g is the acceleration of gravity, h is the height of squatting, which is around

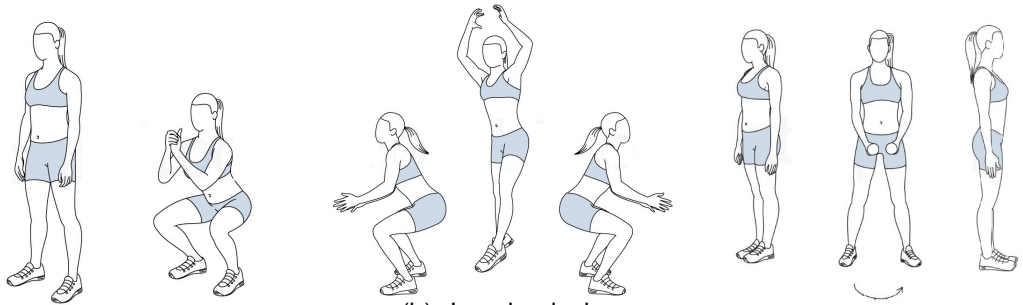

(a) Squatting (b) Jumping jacks (c) circling around

Figure 3.4: Exercise sketches

half of the human height, here is 0.8 m. Thus, the fastest speed during the squat is 3.9m/s and the movement speed of the arms can be ignored. During the simulation time(5s), the whole event repeats twice.

Jumping Jacks are more complex, involving the movement of the arms, thighs and torso. During take-off, the arms lift up, the thighs spread out to the sides and the body moves upward. While the process of descending is to lower the arms, close the thighs and squat down the body. Similar to squatting, the faster speed happens in the process of the body moving up and down. Based on equation3.2, assuming $h = 0.4m$, v should be around 2.9m/s. And the period of jumping Jacks is 2s.

As for turning in a circle, that is, the person rotates the body clockwise or counterclockwise at a constant speed. Since the body is doing approximate circular motion [62], it is necessary to use the angular velocity formula

$$\omega = 2\pi f_r \tag{3.3}$$

$$v = \omega r \tag{3.4}$$

where f_r is the rotating speed,r is the rotation radius. In the experiment, $f_r = 0.4rad/s$,$r = 0.5m$, so $v \approx 1.26m/s$.

According to the above analysis, it can be found that the maximum Doppler shift and the time interval of the adjacent maximum movement speed of the three activities are totally different. Therefore, events can be matched based on these characteristics. The specific event-matching method is shown in the next chapter.

Chapter 4

Numerical Analysis

Chapter3 introduced the measurement setup, as well as three events in two scenarios. This chapter displays real measurement results and analyzed the impact of testbed configurations on event matching.

4.1 Performance metrics

To evaluate the performance of the testbed, I employed two metrics: Maximum Doppler shift ($\Delta f_{Doppler,max}$) and the time difference between adjacent peak amplitude (ΔT_{pp}).

According to section 3.2.2, the maximum speeds among the three events are totally different. Theoretically, $\Delta f_{Doppler,max}$ should also be different in three activities and $\Delta f_{Doppler,max}(squat) > \Delta f_{Doppler,max}(jumpingjacks) > \Delta f_{Doppler,max}(circling)$. Besides, the transmitted signal strength is affected by motion relative speed, angle and location. And three events involved in body parts, body movement duration and frequency are also different(see section 3.2.2). Thus,ΔT_{pp} is a reliable metric of HAR.

In order to obtain the accuracy of metrics, confidential interval(CI) is applied to measure the certainty that the $\Delta f_{Doppler,max}$ and ΔT_{pp} obtained by each measurement are within a certain range [63].

$$CI = \overline{S} \pm \chi \frac{std}{\sqrt{n}} \tag{4.1}$$

Where $\overline{S}$ is the average of $n = 20$ experimental results, std is the standard deviation of 20 times measurements, $\chi = 2.326$ is the confidence level that the result has 98% probability of falling within the CI. It reflected the reliability of the testbed and performance metrics.

4.2 Numerical Examples

4.2.1 Event Matching at Concurrent Dual-band

As described in section 4.1, $\Delta f_{Doppler,max}$and ΔT_{pp} are unique and different across the three events in the same antenna scenario. Figure 4.1 is an example of channel $[2, 2]$ three human activities Doppler variant transform function in the orthogonal scenario at 560ksps, 1.25Msps and 2Msps sampling rate. Each line in the figure represents an OFDM symbol. Since each OFDM signal includes 1024 OFDM symbols, within the simulation time (5s), there are 1,155,648, 97,280, and 438,272 OFDM symbols at the sampling rates of 2Msps, 1.25Msps, and 560ksps respectively. It's obvious that $\Delta f_{Doppler,max}$ of three events are totally different and they are unlike at three sampling rates under the same activities.

Because 52 out of 64 SCs are data, the valid SCs are 52 per OFDM symbol. Here, we choose the 21st SC as an example, where the Time variant impulse responses of the 21st SC of all channels, events and scenarios at 560ksps sampling rate is shown in Figure 4.2. The results show that ΔT_{pp} works on the different channels under the same scenario. That's because the movement that causes the largest amplitude variation is fixed. The different channels only change the absolute amplitude(eg, peak or trough in Figure 4.2 c), but do not change the relative time duration between the two largest movements. In fact, different carrier frequencies also keep the same ΔT_{pp} at equal sampling rates. Similarly, the Doppler shift of each channel doesn't change. The selection of the channel only changes the energy of the Doppler shift.

Therefore, we can calculate twelve different CI of $\Delta f_{Doppler,max}$ based on a double band, three sampling rates and two scenarios for each event. And ΔT_{pp} use six(three sampling rates, two scenarios) reliable intervals for each event. HAR can be performed by comparing and matching the measured $\Delta f_{Doppler,max}$ and ΔT_{pp} with a series of pre-determined intervals. If the measured value falls within one of the intervals, the event is matched. Otherwise, there's no event matched.

Based on this rule, event-matching accuracy per metric can be written as

$$Accuracy = \frac{P_{true}}{P_{true} + P_{false} + P_{non}} \tag{4.2}$$

where P_{true} represents the number of signals that are correctly classified into the events(squatting, jumping Jacks, circling around) according to performance metrics ($\Delta f_{Doppler,max}$ or ΔT_{pp}). P_{false} is the number of signals that are incorrectly classified into events based on performance metrics. P_{non} is the number of signals that could not be classified into any events. In order to enhance the classification accuracy, the

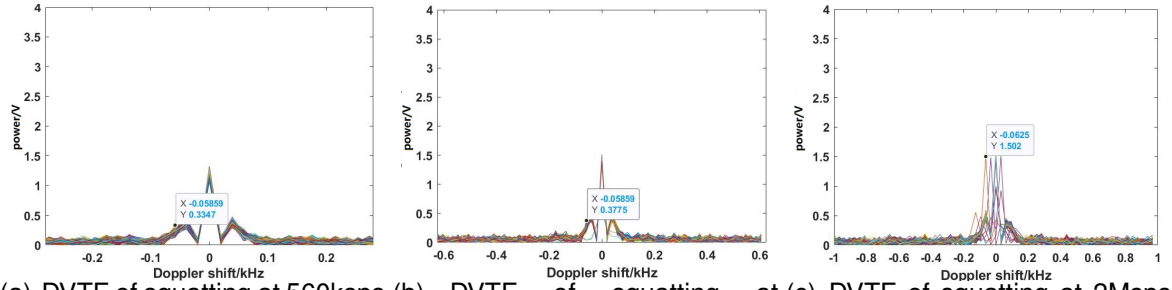

(a) DVTF of squatting at 560ksps sample rate (b) DVTF of squatting at 1.25Msps sample rate (c) DVTF of squatting at 2Msps sample rate

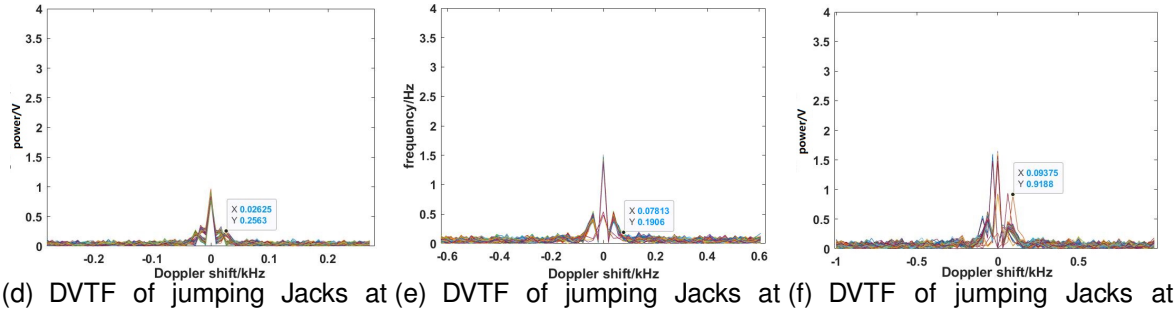

(d) DVTF of jumping Jacks at 560ksps sample rate (e) DVTF of jumping Jacks at 1.25Msps sample rate (f) DVTF of jumping Jacks at 2Msps sample rate

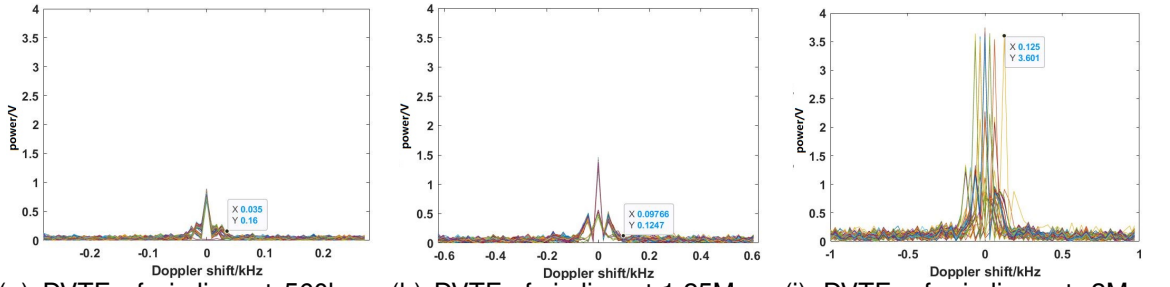

(g) DVTF of circling at 560ksps sample rate (h) DVTF of circling at 1.25Msps sample rate (i) DVTF of circling at 2Msps sample rate

Figure 4.1: TX2 to RX2 channel Doppler Variant Transfer Function(DVTF) of three events of three sampling rates in orthogonal scenario

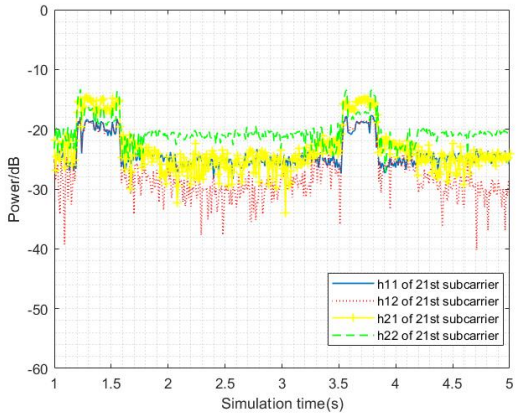

(a) Time Variant impulse response of squat up in perpendicular scenario

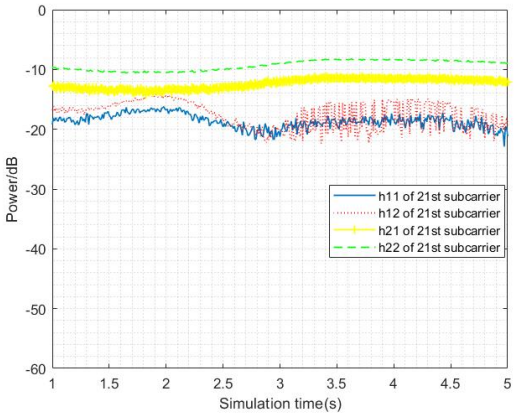

(b) Time Variant impulse response of squat up in parallel scenario

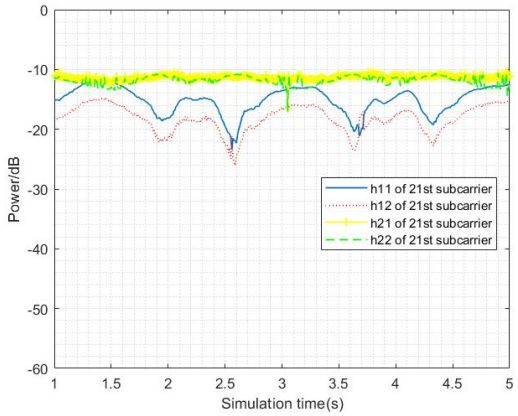

(c) Time Variant impulse response of jumping Jacks in perpendicular scenario

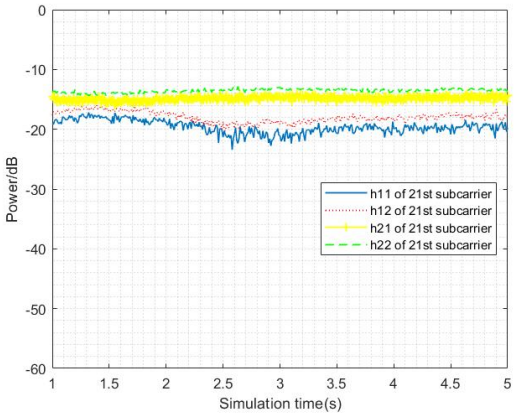

(d) Time Variant impulse response of jumping Jacks in parallel scenario

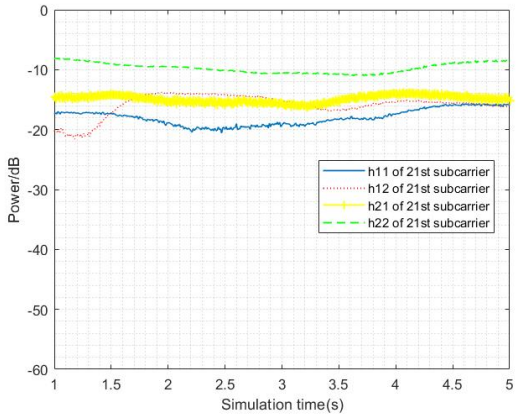

(e) Time Variant impulse response of circling around in perpendicular scenario

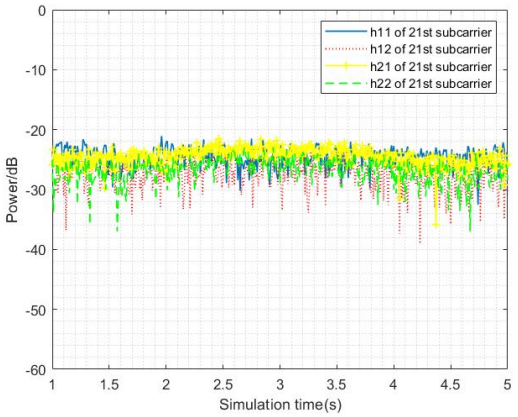

(f) Time Variant impulse response of circling around in parallel scenario

Figure 4.2: 900MHz signal Time Variant impulse response of 21st subcarrier of three events of 560ksps sampling rate in two scenario

Type of Events	Squatting		Jumping Jacks		Circling around	
Metrics	$\Delta f_{Doppler,max}$	ΔT_{pp}	$\Delta f_{Doppler,max}$	ΔT_{pp}	$\Delta f_{Doppler,max}$	ΔT_{pp}
Accuracy(%)	88.125	98.125	92.500	78.750	96.250	81.875
Overall Accuracy(%)	99.375		98.750		97.500	

Table 4.1: Overall accuracy of three events of dual-band of orthogonal antenna array layout at 1.25Msps sampling rate with two metrics

two performance metrics can be used comprehensively. Thus, the overall accuracy is

$$Overall\ Accuracy = \frac{P_{true,MaxDoppler} + P_{true,pp}}{P_{true,MaxDoppler} + P_{true,pp} + P_{false,Dpp} + P_{non,Dpp}} \tag{4.3}$$

where $P_{true,MaxDoppler}$ is the number of signals that are correctly classified into the events by $\Delta f_{Doppler,max}$, $P_{true,pp}$ is the number of signals correctly classified as events by the ΔT_{pp} among signals incorrectly classified by $\Delta f_{Doppler,max}$ and not classified into any events(that is $P_{false,Doppler} + P_{non,Doppler}$). $P_{false,Dpp}$ is the number of signals that are still unclassified into events after using both $\Delta f_{Doppler,max}$ and ΔT_{pp}. $P_{non,Dpp}$ is the number of signals that could not be classified into any events by two performance metrics.

According to equation 4.2 and 4.3, all configuration accuracy of each metric can be calculated. Combined frequency band, sampling rate and TRx antenna array layout, the highest event matching accuracy can be achieved when using dual-band, 1.25Msps sampling rate and orthogonal antenna layout(Discuss in later sections). Table 4.1 shows the event-matching accuracy of the above configurations. Results perform that squatting has the highest overall event-matching accuracy of 99.38% and the highest event-matching accuracy of 98.14% of ΔT_{pp}. Because squatting has the highest $\Delta f_{Doppler,max}$ and simplest action composition. The average event-matching accuracy of three events is $\frac{99.375+98.750+97.500}{3}\% \approx 98.54\%$.

The possible reason why the three events have mismatched

(a) 98% confidence level means there is still 2% probability that the measured value is outside the CI.

(b) The metrics of evaluating event matching are not good enough. In some setups, it might occur similar results of different activities.

(c) The approach of extracting signals is something to improve. Figure 4.2 shows that the amplitude has some jitters from the environment (it's hard to guarantee a real static environment). Increasing the use of some filters (like wavelet filters) can alleviate the influence of the external environment.

Impact of Concurrent Double-Band

Based on equation 2.4, transmission frequency and the direction of motion with respect to the receiver determine the Doppler shift. Under the same configuration and motion, a high-frequency signal has a higher Doppler resolution. Some movement only can be captured by 5.8GHz carrier frequency. That's why higher frequency has more Doppler shift. Moreover, the higher carrier frequency has more signal attenuation. 5.8GHz signal has around 20dB path loss of more than 900MHz. Hence, there is more fluctuation of CSI for 5.8GHz frequency. We could not distinguish the amplitude variation of small motion, especially for higher frequency. Combining the characteristics of high and low frequency, human activities can be better identified.

Table 4.2 compares the two single-band(900MHz, 5.8GHz) recognition abilities with double-band, where the red number is the maximum event-matching accuracy of two frequency bands based on two performance metrics. The accuracy of metric on the dual band can be calculated as

$$Accuracy\ of\ metric = \frac{P_{true,5.8GHz} + P_{true,900MHz}}{P_{true,5.8GHz} + P_{true,900MHz} + P_{false,dual} + P_{non,dual}} \tag{4.4}$$

where $P_{true,5.8GHz}$ is the number of signals that are correctly classified into the events on the 5.8GHz frequency band by performance metrics($\Delta f_{Doppler,max}$ or $P_{true,pp}$), $P_{true,900MHz}$ is the number of signals correctly classified as events on the 900MHz frequency band by the determined performance metric among signals incorrectly classified by the same performance metric on the 5.8GHz frequency band and not classified into any events(that is $P_{false,5.8GHz} + P_{non,5.8GHz}$). $P_{false,dual}$ is the number of signals that are still unclassified into events after using dual-band signals with the same performance metric. $P_{non,dual}$ is the number of signals that could not be classified into any events by two frequencies with the same performance metric. The overall accuracy of the double-band uses the equation 4.3 and the event-matching accuracy of each frequency band is calculated by equation 4.2.

The table 4.2 shows that double-band performance is better than two single bands no matter using which performance metric. It contains two antenna array layouts, three sampling rates, and all signals on four channels. Because high-frequency signals have shorter wavelengths and higher Doppler resolution, smaller Doppler shifts and amplitude fluctuations that cannot be captured by low-frequency signals can be recorded by high-frequency signals. For $\Delta f_{Doppler,max}$, within the range of Maximum unambiguous Doppler, the larger the Doppler frequency shift, the easier it is to be identified. For ΔT_{pp}, the smaller the amplitude jitter, the more accurate the selection of the two peaks. Therefore, high-frequency signals are suitable for $\Delta f_{Doppler,max}$, while low-frequency signals are suitable for ΔT_{pp}. The simultaneous utility of dual bands means that the benefits of both the high and low bands can

Type of Events		Squatting		Jumping Jacks		Circling around	
Metrics		$\Delta f_{Doppler,max}$	ΔT_{pp}	$\Delta f_{Doppler,max}$	ΔT_{pp}	$\Delta f_{Doppler,max}$	ΔT_{pp}
5.8GHz	Accuracy of Metric(%)	79.81	14.59	87.21	13.26	47.27	34.59
900MHz		52.01	89.53	38.65	76.45	50.94	61.01
Double-band		89.92	89.53	89.42	76.45	77.84	65.83
	Overall Accuracy(%)	97.95		96.44		94.19	

Table 4.2: Effect of double-band on event-matching accuracy

be applied simultaneously when one band selects high frequencies and the other selects low frequencies. While a signal in the 5.8GHz band cannot match an event, it is quite possible that a 900MHz signal that is simultaneously recorded can match an event or vice versa. This also explains why the event-matching accuracy of the two evaluation criteria in table 4.2 varies greatly on different frequency bands.

However, the fact that the 900MHz frequency signal is optimized over 5.8GHz frequency is counter-intuitive on the whole. It indicates that amplitude jitters influence on high-frequency is large than low Doppler resolution effect on low-frequency. Besides, the overall accuracy of events is, $Q_{squatting} > Q_{jumpingJacks} > Q_{circlingaround}$. That's because the more simple and more high-speed motion is easier to match. The average event-matching accuracy of three event on dual-band is $\frac{97.95+96.44+94.19}{3}\% \approx 96.19\%$.

Impact of sampling rate

The sampling rate is defined as the number of samples taken per second from a continuous signal to generate digital/discrete signals [64]. The Nyquist frequency is equal to half of the sample rate, which should be greater than the highest frequency that needs to be preserved [45]. Thus a higher sampling rate could collect higher frequency with more information. However, a higher sampling rate causes a longer time delay due to the limited buffer size. Excessive delay results in incomplete CSI.

BladeRF RX sampling rate is locked to 553.6ksps to 2Msps for the Simulink Receiver [53].In order to evaluate the impact of BladeRF sampling rate on event matching accuracy under the Simulink platform, this paper selects the highest, lowest and intermediate sampling rates within the allowable range of rates, which are 560ksps,1.25Msps and 2Msps.

Table 4.3 displays the effect of sampling rate on event-matching accuracy, where the red number is the maximum event-matching accuracy under the three sampling rates. The datasets contain two frequency bands, two antenna array layouts (see section 3.2.1) and four channels (2x2 MIMO) of three events at 560ksps,1.25Msps and 2Msps sampling rates separately. For all events, squatting has the highest event-matching accuracy at 1.25Msps, because squatting has the simplest motion (squat up and down) and highest instantaneous speed (see section 3.2.2),

Type of Events		Squatting		Jumping Jacks		Circling around	
Metrics		$\Delta f_{Doppler,max}$	ΔT_{pp}	$\Delta f_{Doppler,max}$	ΔT_{pp}	$\Delta f_{Doppler,max}$	ΔT_{pp}
Accuracy of Metric(%)	560ksps	73.13	51.93	60.72	43.55	37.50	71.94
	1.25Msps	65.64	52.02	64.08	46.63	52.83	53.03
	2Msps	58.97	52.22	63.99	44.38	56.98	18.43
Overall Accuracy(%)	560ksps	90.98		78.28		84.48	
	1.25Msps	91.24		87.84		80.75	
	2Msps	71.78		80.39		63.11	

Table 4.3: Effect of sampling rate on event-matching accuracy

$\Delta f_{Doppler,max}$ is the easiest to be distinguished. And 900MHz signals have a lower frequency shift than 5.8GHz signals(see section 3.1) for the same event, some motion is invisible to 900MHz signals. That's why the event-matching accuracy of $\Delta f_{Doppler,max}$ is low at the different sampling rates. Similarly, the event-matching accuracy of ΔT_{pp} is also terrible at three sampling rates. High-frequency signals (shorter wavelength) would record more CSI than low-frequency signals. It means that the frequency of 5.8GHz has more fluctuations reflected in the amplitude, which increases the probability of selecting the wrong peak-to-peak time interval.

Both squatting and jumping Jacks have the highest event-matching accuracy at 1.25Msps while the circling round is 560ksps. According to section 3.2.2, circling around has a more complex variation. Thus, a lower sampling rate only records the motions, which have a large effect on amplitude.

Because the 1.25Msps sampling rate has the highest average event-matching accuracy, which is 86.61%($\frac{91.24+87.84+84.48}{3}\%$), it is the best choice among three sampling rates. However, its event-matching accuracy is still not high. For increasing average event-matching accuracy, investigating more sampling rates could be the future work.

Impact of TRx antenna array layout

This thesis provides two types of antenna layout, orthogonal(Figure 3.1) and parallel(Figure 3.2). The relative position of the TX and RX antennas is orthogonal means that the transmission path has an angle in the indoor environment. In this case, the movement of the human body in a non-orthogonal direction relative to the RX can significantly change the transmission path of the signal. Therefore, in this scenario, even with a relatively slow speed, the variation in amplitude is still very noticeable. While the parallel setup performance more relies on the direction of human torso motion.

Table 4.4 reveals that the orthogonal antenna array scenario has higher event-matching accuracy than the parallel scenario, where the red number is the maximum event-matching accuracy under two TRx antenna array layouts. Circling around has the highest overall accuracy 98.73%, which is slightly higher than squatting

Type of Events		Squatting		Jumping Jacks		Circling around	
Metrics		$\Delta f_{Doppler,max}$	ΔT_{pp}	$\Delta f_{Doppler,max}$	ΔT_{pp}	$\Delta f_{Doppler,max}$	ΔT_{pp}
Accuracy of Metric(%)	Orthogonal	79.12	54.43	60.07	50.83	56.87	40.63
	Parallel	52.71	49.69	65.79	38.88	41.34	54.96
Overall Accuracy(%)	Orthogonal	98.08		98.56		98.73	
	Parallel	97.88		90.65		95.99	

Table 4.4: Effect of antenna layout on event-matching accuracy

and jumping Jacks. It is worth noting that the overall event-matching accuracy of the jumping Jacks is significantly improved in the orthogonal antenna array layout compared with the parallel antenna layout. It is because most of the motion direction of jumping Jacks is nearly perpendicular to the RX on the parallel antenna array layout. The maximum average event-matching accuracy of three events is $\frac{98.08+98.56+98.73}{3}\% \approx 98.46\%$ on an orthogonal antenna array scenario.

Chapter 5

Conclusion and Recommendation

5.1 Conclusions

In this thesis, we design and implement a JCAS concurrent double-band 2x2 MIMO-OFDM testbed system on an SDR platform, which achieves human activity recognition. The main contributions of this study are (a) the first-time to use BladeRF 2.0 on the MATLAB platform to realize the simultaneous implementation of two 2X2 MIMO so far. (b) use maximum Doppler shift and peak-to-peak amplitude difference to recognize human exercises in the narrowed band and evaluate dual-band, sampling rate and antenna layout effects on recognition.

In Chapter 1, I briefly introduce the background knowledge of MIMO-OFDM, 802.11 standards and CSI.

Chapter 2 initially presents the CSI preprocessing algorithms and the Doppler extraction formula. After comparing the commonly used SDR and its operating platform on the market, the design of the physical layer transceiver is given. It concludes the design of the frame structure, the algorithms involved in all TX and RX blocks and the clock synchronization implementation on the SDR and SDR platform. After completing all designs, the performance of the testbed is verified.

In Chapter 3, the testbed setup are presented, including OFDM ”radar” specifications and the BladeRF configurations. Besides, it discusses the possible outcomes of actually measured of three events in two scenarios.

In Chapter 4, the event matching results and analysis are proposed. Initially, the evaluation metrics for HAR are given. Then it shows some examples of the Doppler variant transforms function and time-variant impulse response of three events. Results indicate that the system can achieve average event-matching accuracy of 98.54% with dual-band, 1.25ksps sampling rate in orthogonal TRx antenna layout, where squatting has the highest event-matching accuracy among three events. The system shows that 5.8GHz frequency signals are suitable for matching events using Doppler shifts, while 900MHz frequency signals are suitable for using CSI amplitude.

Using dual-band signals simultaneously can significantly improve event-matching accuracy by nearly 10%. And the average event-matching accuracy of dual-band is 96.19%. When the sampling rate is 1.25Msps, squatting and jumping Jacks can achieve the largest event-matching accuracy, which is 91.24%, and 87.84%, respectively. The average matching accuracy of the three events is 86.61% in this case, which indicates that none of the sampling rates selected in the thesis is the best choice. Orthogonal antenna array layout has higher event-matching accuracy than parallel antenna layout, and its average event-matching accuracy is 98.46%. The sampling rate has a greater impact on matching accuracy than the antenna layout.

5.2 Recommendation

Taking into account the drawbacks of the above conclusions and the problems encountered in the research, future work can be studied from the following perspectives:

1. The current experimental environment is in a single lab environment, the experiment can be extended to an unrestricted environment, such as a complex office area and pantry. Is the current system's HAR capable in the presence of a large amount of external interference?

2. The three activities are all performed by the same person. If different people perform the same action, whether the evaluation metrics are still able to identify the events performed?

3. When multiple people perform different actions in the experimental space, can the system distinguish them and recognize actions?

4. Due to the limitations of BladeRF on the MATLAB/Simulink platform, the system cannot achieve high Doppler and range resolution. Thus, it cannot recognize fine-grained human activities and locate humans. Can the algorithm be optimized to identify the micro-motion of humans(like a heartbeat) and locate humans?

Bibliography

[1] U. Tamer, "Testbed implementation of a mimo-ofdm data link at sub 6 ghz frequency bands using an sdr platform," Master's thesis, Middle East Technical University, 2018.

[2] M. B. Khan, X. Yang, A. Ren, M. A. M. Al-Hababi, N. Zhao, L. Guan, D. Fan, and S. A. Shah, "Design of software defined radios based platform for activity recognition," *IEEE Access*, vol. 7, pp. 31 083–31 088, 2019.

[3] T. Zhang, T. Song, D. Chen, T. Zhang, and J. Zhuang, "Wigrus: A wifi-based gesture recognition system using software-defined radio," *IEEE Access*, vol. 7, pp. 131 102–131 113, 2019.

[4] Y. Li, F. Shu, B. Shi, X. Cheng, Y. Song, and J. Wang, "Enhanced rss-based uav localization via trajectory and multi-base stations," *IEEE Communications Letters*, vol. 25, no. 6, pp. 1881–1885, 2021.

[5] S. Liu, X. Wang, O. Hassanin, X. Xu, M. Yang, D. Hurwitz, and X. Wu, "Calibration and evaluation of responsibility-sensitive safety (rss) in automated vehicle performance during cut-in scenarios," *Transportation research part C: emerging technologies*, vol. 125, p. 103037, 2021.

[6] S. Tan, Y. Ren, J. Yang, and Y. Chen, "Commodity wifi sensing in 10 years: Status, challenges, and opportunities," *IEEE Internet of Things Journal*, 2022.

[7] S. A. Bhat, A. Mehbodniya, A. E. Alwakeel, J. Webber, and K. Al-Begain, "Human motion patterns recognition based on rss and support vector machines," in *2020 IEEE Wireless Communications and Networking Conference (WCNC)*. IEEE, 2020, pp. 1–6.

[8] *iyush Thakur, "Wi-Fi Sensing: The new standard will turn wireless devices into sensors capable of gathering data about the people objects bathed in their signals."*, 2021. [Online]. Available: https://www.linkedin.com/pulse/wi-fi-sensing-new-standard-turn-wireless-devices-sensors-thakur-

[9] *electronicsnotes,"IEEE 802.11ac Gigabit Wi-Fi"*, 2022. [Online]. Available: https://www.electronics-notes.com/articles/connectivity/wifi-ieee-802-11/802-11ac.php

[10] *electronicsnotes,"IEEE 802.11ah: sub GHz Wi-Fi"*, 2022. [Online]. Available: https://www.electronics-notes.com/articles/connectivity/wifi-ieee-802-11/802-11ah-sub-ghz-wifi.php

[11] Y. L. Sit, *MIMO OFDM radar-communication system with mutual interference cancellation*. KIT Scientific Publishing, 2017, vol. 82.

[12] Y. S. Cho, J. Kim, W. Y. Yang, and C. G. Kang, *MIMO-OFDM wireless communications with MATLAB*. John Wiley & Sons, 2010.

[13] *Keysight, "Concepts of Orthogonal Frequency Division Multiplexing (OFDM) and 802.11 WLAN"*, 2022. [Online]. Available: https://rfmw.em.keysight.com/wireless/helpfiles/89600B/WebHelp/Subsystems/wlan-ofdm/content/ofdm_basicprinciplesoverview.htm

[14] Y. Ma, G. Zhou, and S. Wang, "Wifi sensing with channel state information: A survey," *ACM Computing Surveys (CSUR)*, vol. 52, no. 3, pp. 1–36, 2019.

[15] D. Sasakawa, N. Honma, T. Nakayama, and S. Iizuka, "Human posture identification using a mimo array," *Electronics*, vol. 7, no. 3, p. 37, 2018.

[16] A. Mohanna, C. Gianoglio, A. Rizik, and M. Valle, "A convolutional neural network-based method for discriminating shadowed targets in frequency-modulated continuous-wave radar systems," *Sensors*, vol. 22, no. 3, p. 1048, 2022.

[17] Y. Xu, W. Yang, J. Wang, X. Zhou, H. Li, and L. Huang, "Wistep: Device-free step counting with wifi signals," *Proceedings of the ACM on Interactive, Mobile, Wearable and Ubiquitous Technologies*, vol. 1, no. 4, pp. 1–23, 2018.

[18] J. Liu, L. Wang, L. Guo, J. Fang, B. Lu, and W. Zhou, "A research on csi-based human motion detection in complex scenarios," in *2017 IEEE 19th International Conference on e-Health Networking, Applications and Services (Healthcom)*. IEEE, 2017, pp. 1–6.

[19] S. Li, X. Li, K. Niu, H. Wang, Y. Zhang, and D. Zhang, "Ar-alarm: An adaptive and robust intrusion detection system leveraging csi from commodity wi-fi," in *Enhanced Quality of Life and Smart Living: 15th International Conference, ICOST 2017, Paris, France, August 29-31, 2017, Proceedings 15*. Springer, 2017, pp. 211–223.

[20] Y. Zhong, J. Wang, S. Wu, T. Jiang, Y. Huang, and Q. Wu, "Multilocation human activity recognition via mimo-ofdm-based wireless networks: An iot-inspired device-free sensing approach," *IEEE Internet of Things Journal*, vol. 8, no. 20, pp. 15 148–15 159, 2021.

[21] K. Ohara, T. Maekawa, S. Sigg, and M. Youssef, "Preliminary investigation of position independent gesture recognition using wi-fi csi," in *2018 IEEE International Conference on Pervasive Computing and Communications Workshops (PerCom Workshops)*. IEEE, 2018, pp. 480–483.

[22] K. Ali, A. X. Liu, W. Wang, and M. Shahzad, "Recognizing keystrokes using wifi devices," *IEEE Journal on Selected Areas in Communications*, vol. 35, no. 5, pp. 1175–1190, 2017.

[23] S. M. Bokhari, S. Sohaib, A. R. Khan, M. Shafi *et al.*, "Dgru based human activity recognition using channel state information," *Measurement*, vol. 167, p. 108245, 2021.

[24] Y. Wang, K. Wu, and L. M. Ni, "Wifall: Device-free fall detection by wireless networks," *IEEE Transactions on Mobile Computing*, vol. 16, no. 2, pp. 581–594, 2016.

[25] F. Zhang, C. Chen, B. Wang, and K. R. Liu, "Wispeed: A statistical electromagnetic approach for device-free indoor speed estimation," *IEEE Internet of Things Journal*, vol. 5, no. 3, pp. 2163–2177, 2018.

[26] S. Palipana, D. Rojas, P. Agrawal, and D. Pesch, "Falldefi: Ubiquitous fall detection using commodity wi-fi devices," *Proceedings of the ACM on Interactive, Mobile, Wearable and Ubiquitous Technologies*, vol. 1, no. 4, pp. 1–25, 2018.

[27] S. Arshad, C. Feng, Y. Liu, Y. Hu, R. Yu, S. Zhou, and H. Li, "Wi-chase: A wifi based human activity recognition system for sensorless environments," in *2017 IEEE 18th International Symposium on A World of Wireless, Mobile and Multimedia Networks (WoWMoM)*. IEEE, 2017, pp. 1–6.

[28] M. De Sanctis, E. Cianca, S. Di Domenico, D. Provenziani, G. Bianchi, and M. Ruggieri, "Wibecam: Device free human activity recognition through wifi beacon-enabled camera," in *Proceedings of the 2nd workshop on Workshop on Physical Analytics*, 2015, pp. 7–12.

[29] Y. Jin, Z. Tian, M. Zhou, Z. Li, and Z. Zhang, "A whole-home level intrusion detection system using wifi-enabled iot," in *2018 14th International Wireless Communications & Mobile Computing Conference (IWCMC)*. IEEE, 2018, pp. 494–499.

[30] D. Wu, D. Zhang, C. Xu, H. Wang, and X. Li, "Device-free wifi human sensing: From pattern-based to model-based approaches," *IEEE Communications Magazine*, vol. 55, no. 10, pp. 91–97, 2017.

[31] R. Zhou, X. Lu, P. Zhao, and J. Chen, "Device-free presence detection and localization with svm and csi fingerprinting," *IEEE Sensors Journal*, vol. 17, no. 23, pp. 7990–7999, 2017.

[32] Z. Zhou, Z. Yang, C. Wu, L. Shangguan, and Y. Liu, "Omnidirectional coverage for device-free passive human detection," *IEEE Transactions on Parallel and Distributed Systems*, vol. 25, no. 7, pp. 1819–1829, 2013.

[33] E. Cardillo and A. Caddemi, "A review on biomedical mimo radars for vital sign detection and human localization," *Electronics*, vol. 9, no. 9, p. 1497, 2020.

[34] P. Wang, B. Guo, T. Xin, Z. Wang, and Z. Yu, "Tinysense: Multi-user respiration detection using wi-fi csi signals," in *2017 IEEE 19th International Conference on e-Health Networking, Applications and Services (Healthcom)*. IEEE, 2017, pp. 1–6.

[35] X. Liu, J. Cao, S. Tang, J. Wen, and P. Guo, "Contactless respiration monitoring via off-the-shelf wifi devices," *IEEE Transactions on Mobile Computing*, vol. 15, no. 10, pp. 2466–2479, 2015.

[36] Q. Pu, S. Gupta, S. Gollakota, and S. Patel, "Whole-home gesture recognition using wireless signals," ser. MobiCom '13. New York, NY, USA: Association for Computing Machinery, 2013, p. 27–38.

[37] M. Li, Y. Meng, J. Liu, H. Zhu, X. Liang, Y. Liu, and N. Ruan, "When csi meets public wifi: inferring your mobile phone password via wifi signals," in *Proceedings of the 2016 ACM SIGSAC conference on computer and communications security*, 2016, pp. 1068–1079.

[38] H. Li, W. Yang, J. Wang, Y. Xu, and L. Huang, "Wifinger: Talk to your smart devices with finger-grained gesture," in *Proceedings of the 2016 ACM International Joint Conference on Pervasive and Ubiquitous Computing*, 2016, pp. 250–261.

[39] J. He, S. Terashima, H. Yamada, and S. Kidera, "Diffraction signal-based human recognition in non-line-of-sight (nlos) situation for millimeter wave radar," *IEEE Journal of Selected Topics in Applied Earth Observations and Remote Sensing*, vol. 14, pp. 4370–4380, 2021.

[40] O. Rabaste, J. Bosse, D. Poullin, I. Hinostroza, T. Letertre, T. Chonavel *et al.*, "Around-the-corner radar: Detection and localization of a target in non-line of sight," in *2017 IEEE Radar Conference (RadarConf)*. IEEE, 2017, pp. 0842–0847.

[41] M. B. Khalilsarai, B. Gross, S. Stefanatos, G. Wunder, and G. Caire, "Wifi-based channel impulse response estimation and localization via multi-band splicing," in *GLOBECOM 2020 - 2020 IEEE Global Communications Conference*, 2020, pp. 1–6.

[42] V. Winkler, D. Fränken, C. Erhart, O. Zeeb, and S. Lutz, "Multistatic multiband passive radar-architecture and sensor cluster results," in *2019 IEEE Radar Conference (RadarConf)*. IEEE, 2019, pp. 1–6.

[43] G. Serafino, S. Maresca, L. Di Mauro, A. Tardo, A. Cuillo, F. Scotti, P. Ghelfi, P. Pagano, and A. Bogoni, "A photonics-assisted multi-band mimo radar network for the port of the future," *IEEE Journal of Selected Topics in Quantum Electronics*, vol. 27, no. 6, pp. 1–13, 2021.

[44] D. Franken, T. Ott, S. Lutz, F. Hoffmann, P. Samczinski, M. Plotka, M. Drozka, C. Schupbach, Z. Mathews, S. Welschen *et al.*, "Integrating multiband active and passive radar for enhanced situational awareness," *IEEE Aerospace and Electronic Systems Magazine*, 2022.

[45] M. Al-Rahbi, "Human activity recognition using channel state information," 2019.

[46] A. Goldsmith, *Wireless communications*. Cambridge university press, 2005.

[47] R. W. Stewart, K. W. Barlee, D. S. Atkinson, and L. H. Crockett, *Software defined radio using MATLAB & Simulink and the RTL-SDR*, 2015.

[48] *Nuand, "bladeRF 2.0 micro xA9"*, 2022. [Online]. Available: https://www.nuand.com/product/bladeRF-xA9/

[49] *RTL-SDR.com, "RTL-SDR Blog V3 Datasheet"*, 2020. [Online]. Available: https://www.rtl-sdr.com/wp-content/uploads/2018/02/RTL-SDR-Blog-V3-Datasheet.pdf

[50] *Lime Microsystems, "LimeSDR Mini 2.0 — Crowd Supply"*, 2022. [Online]. Available: https://www.crowdsupply.com/lime-micro/limesdr-mini-2

[51] *Jose.Amador, "BladeRF_MIMO"*, 2021. [Online]. Available: https://github.com/JoseAmador95/BladeRF_MIMO

[52] *Nuand,"libbladeRF 2.2.1"*, 2019. [Online]. Available: https://www.nuand.com/bladeRF-doc/libbladeRF/v2.2.1/

[53] *Victor.Bursucianu,"Communications Toolbox Support Package for BladeRF 2.0"*, 2020. [Online]. Available: https://www.mathworks.com/matlabcentral/fileexchange/74591-communications-toolbox-support-package-for-bladerf-2-0

[54] *Mouser Electronics,"TG.45.8113W Apex III 4G 450MHz to 6GHz LTE Dipole Terminal Antenna Datasheet"*, 2022. [Online]. Available: https://www.mouser.com/datasheet/2/398/TG.45.8113W-1508737.pdf

[55] *Martin Clark, "IEEE 802.11a WLAN model"*, 2016. [Online]. Available: https://www.mathworks.com/matlabcentral/fileexchange/3540-ieee-802-11a-wlan-model

[56] P. J. Beasley and M. A. Ritchie, "bladerad: Development of an active and passive, multistatic enabled, radar system," in *2021 18th European Radar Conference (EuRAD)*. IEEE, 2022, pp. 98–101.

[57] C. N. Kishore and V. U. Reddy, "A frame synchronization and frequency offset estimation algorithm for ofdm system and its analysis," *EURASIP Journal on Wireless Communications and Networking*, vol. 2006, no. 1, p. 057018, 2006.

[58] H. Yuan, X. Hu, and Y. Ling, "New symbol synchronization algorithms for ofdm systems based on ieee 802.11 a," in *2008 6th IEEE International Conference on Industrial Informatics*. IEEE, 2008, pp. 186–191.

[59] S. R. Chaudhary, A. J. Patil, and A. V. Yadao, "Wlan-ieee 802.11 ac: Simulation and performance evaluation with mimo-ofdm," in *2016 Conference on Advances in Signal Processing (CASP)*. IEEE, 2016, pp. 440–445.

[60] *Garcia D, "Robust smoothing of gridded data in one and higher dimensions with missing values"*, 2010. [Online]. Available: http://www.biomecardio.com/pageshtm/publi/csda10.pdf

[61] *Bogna Szyk, "Simple Pendulum Calculator"*, 2022. [Online]. Available: https://www.omnicalculator.com/physics/simple-pendulum

[62] T. Matsui, M. Motegi, and N. Tani, "Mathematical model for simulating human squat movements based on sequential optimization," *Mechanical Engineering Journal*, vol. 3, no. 2, pp. 15–00 377, 2016.

[63] B. R. Haverkort, *Performance of computer communication systems: a model-based approach*. John Wiley & Sons, Inc., 1998.

[64] C. Liu, “Radar and communication signal processing algorithm and implementation using ofdm based waveform,” Master’s thesis, 2018.

Appendix A

BladeRF Clock Synchronization Code in MATLAB/Simulink

This section lists the key code of double BladeRFs clock synchronization, including reference clock functions and system object of MIMO BlaadRF block in Simulink. This code could expand to multiple BladeRFs clock synchronization in both MATLAB and Simulink platform.

A.1 BladeRF Reference Clock Configurations

```
classdef bladeRF_Misc < handle

    properties(SetAccess=immutable, Hidden=true)
        bladerf
    end

    properties(SetAccess=immutable)
        dc_power            %Read current power consumption
        dc_source           %Read DC power source
        temperature         %Read current temperature in 'C
    end

    properties(Dependent = true)
        ref_status
        ref_freq
    end

    methods
```

```
19          function set.ref_status(obj,val)
20              val_bool = true(val);
21              status = calllib('libbladeRF', '
                    bladerf_set_pll_enable', obj.bladerf.device,
                    val,val_bool);
22              bladeRF.check_status('bladerf_set_pll_enable',
                    status);
23          end
24          function set.ref_freq(obj,val)
25              val_64 = uint64(val);
26              status = calllib('libbladeRF', '
                    bladerf_set_pll_refclk', obj.bladerf.device,
                    val,val_64);
27              bladeRF.check_status('bladerf_set_pll_refclk',
                    status);
28          end
29          function ref_s = get.ref_status(obj)
30              ref_s = true(1);
31              [status,~,ref_s]= calllib('libbladeRF', '
                    bladerf_get_pll_enable', obj.bladerf.device,
                    ref_s);
32              bladeRF.check_status('bladerf_get_pll_enable',
                    status);
33          end
34          function val_freq = get.ref_freq(obj)
35              val_freq = uint64(0);
36              [status,~,val_freq]=calllib('libbladeRF', '
                    bladerf_get_pll_refclk', obj.bladerf.device,
                    val_64);
37              bladeRF.check_status('bladerf_get_pll_refclk',
                    status);
38          end
39      end
40  end
```

A.2 MIMO BladeRF System Object in Simulink Block

```
1  classdef bladeRF_MIMO_Simulink < matlab.System & ...
```

```
                                matlab.system.mixin.Propagates &
                                    ...
                                matlab.system.mixin.CustomIcon
    %properties
        verbosity           = 'Info'    %libbladeRF verbosity

        rx_frequency        = 890e6;    %Frequency (Hz)
        rx_gain             = [60  60];         %RX Gain [-10, 90]
        rx_agc              = 'SLOW';   %AGC mode

        tx_frequency        = 890e6;    %Frequency (Hz)
        tx_gain             = [60  60]; %TX Gain [-10, 60]
    end
    properties(Logical, Nontunable)
        enable_ref_status   = true;
        enable_rx           = true;     %Enable Receiver
        enable_rx_biastee   = false;    %Enable RX Biastee
        enable_overrun      = false;    %Enable Overrun output
        enable_tx           = true;     %Enable Transmitter
        enable_tx_biastee   = false;    %Enable TX Biastee
        enable_underrun     = false;    %Enable Underrun output
            (for future use)
        xb200               = false     %Enable use of XB-200
            (must be attached)
    end
    properties (Access = private)
        device = []

        %Cache previously set tunable values to avoid querying the device
        %for all properties when only one changes.
        curr_ref_status
        curr_rx_frequency
        curr_rx_lna
        curr_rx_vga1
        curr_rx_vga2
        curr_rx_gain
        curr_rx_agc
        curr_rx_biastee
        curr_tx_frequency
        curr_tx_vga1
```

```
39          curr_tx_vga2
40          curr_tx_gain
41          curr_tx_biastee
42
43      end
44      %methods (Static, Access = protected)
45          function groups = getPropertyGroupsImpl
46              device_section_group = matlab.system.display.
                    SectionGroup(...
47                  'Title', 'Device', ...
48                  'PropertyList', {'device_string', '
                        loopback_mode', 'xb200' } ...
49              );
50
51              rx_gain_section = matlab.system.display.Section
                    (...
52                  'Title', 'Gain', ...
53                  'PropertyList', { 'rx_gain', '
                        enable_rx_biastee', 'rx_agc'  } ...
54              );
55
56              rx_stream_section = matlab.system.display.Section
                    (...
57                  'Title', 'Stream', ...
58                  'PropertyList', {'rx_num_buffers', '
                        rx_num_transfers', 'rx_buf_size', '
                        rx_timeout_ms', 'rx_step_size', } ...
59              );
60
61              rx_section_group = matlab.system.display.
                    SectionGroup(...
62                  'Title', 'RX Configuration', ...
63                  'PropertyList', { 'enable_rx', '
                        enable_overrun', 'rx_frequency', '
                        rx_samplerate', 'rx_bandwidth' }, ...
64                  'Sections', [ rx_gain_section,
                        rx_stream_section ] ...
65              );
66
```

```
67          tx_gain_section = matlab.system.display.Section
               (...
68           'Title', 'Gain', ...
69           'PropertyList', { 'tx_gain', '
                enable_tx_biastee' } ...
70          );
71
72          tx_stream_section = matlab.system.display.Section
               (...
73           'Title', 'Stream', ...
74           'PropertyList', {'tx_num_buffers', '
                tx_num_transfers', 'tx_buf_size', '
                tx_timeout_ms', 'tx_step_size', } ...
75          );
76
77          tx_section_group = matlab.system.display.
               SectionGroup(...
78           'Title', 'TX Configuration', ...
79           'PropertyList', { 'enable_tx', '
                enable_underrun', 'tx_frequency', '
                tx_samplerate', 'tx_bandwidth' }, ...
80           'Sections', [ tx_gain_section,
                tx_stream_section ] ...
81          );
82          misc_section_group = matlab.system.display.
               SectionGroup(...
83           'Title', 'Miscellaneous', ...
84           'PropertyList', {'enable_ref_status','
                verbosity'} ...
85          );
86          groups = [ device_section_group, rx_section_group
               , tx_section_group, misc_section_group ];
87      end
88      function header = getHeaderImpl
89          text = 'This block provides access to a Nuand
               bladeRF device via libbladeRF MATLAB bindings.
               ';
90          header = matlab.system.display.Header('
               bladeRF_Simulink', ...
```

```
91                  'Title', 'bladeRF', 'Text',  text ...
92              );
93          end
94      end
95      methods (Access = protected)
96              %if obj.xb200 == true
97                  xb = 'XB200';
98              else
99                  xb = [];
100             end
101             obj.device = bladeRF_MIMO(obj.device_string, [],
                    xb);
102             obj.device.loopback = obj.loopback_mode;
103             obj.device.misc.ref_status = obj.
                    enable_ref_status;
104             obj.curr_ref_status = obj.device.misc.ref_status;
105         end
106     end
107 end
```